

Anderson localization of electromagnetic waves in three dimensions

Received: 6 September 2022

Accepted: 11 May 2023

Published online: 15 June 2023

 Check for updates

Alexey Yamilov¹✉, Sergey E. Skipetrov², Tyler W. Hughes³,
Momchil Minkov³, Zongfu Yu⁴✉ & Hui Cao⁵✉

Anderson localization is a halt of diffusive wave propagation in disordered systems. Despite extensive studies over the past 40 years, Anderson localization of light in three dimensions has remained elusive, leading to the question of its very existence. Recent advances have enabled finite-difference time-domain calculations to be sped up by orders of magnitude, allowing us to conduct brute-force numerical simulations of light transport in fully disordered three-dimensional systems with unprecedented dimension and refractive index difference. We show numerically three-dimensional localization of vector electromagnetic waves in random aggregates of overlapping metallic spheres, in sharp contrast to the absence of localization for dielectric spheres with a refractive index up to 10 in air. Our work opens a wide range of avenues in both fundamental research related to Anderson localization and potential applications using three-dimensional localized light.

Anderson localization (AL)¹ is an emergent phenomenon for both quantum and classical waves including electron^{2–4}, cold-atom^{5,6}, electromagnetic (EM)^{7–11}, acoustic^{12,13}, water¹⁴, seismic¹⁵ and gravity¹⁶ waves. Unlike in one or two dimensions, AL in three dimensions requires strong disorder^{1,17–19}. A mobility edge separating the diffuse transport regime from AL can be estimated from the Ioffe–Regel criterion $k_{\text{eff}}\ell_s \approx 1$, where k_{eff} is the effective wavenumber in the medium and ℓ_s is the scattering mean free path²⁰. This criterion suggests two avenues to achieving localization: reduction of k_{eff} or ℓ_s . For EM waves, the reduction of k_{eff} is realized by introducing partial order or spatial correlation in the position of scatterers^{7,21}. In comparison, reaching localization of light in fully random photonic media by increasing the scattering strength (decreasing ℓ_s) turns out to be much more challenging^{22,23}. Despite successful experiments in low-dimensional systems^{9,10,24}, three-dimensional (3D) localization remained stubbornly elusive²⁵, which triggered theoretical^{26,27} and experimental²⁸ studies of the mechanisms that impede it.

Anderson himself originally proposed “a system composed essentially of random waveguides near cut-off and random resonators, such as might be realized by a random packing of metallic balls of the right size” as “the ideal system” for localization of EM radiation⁸. In practice,

the absorption of metals obscures localization^{9,29}, and the experimental focus shifted to dielectric materials with low loss and high refractive index^{29–33}. However, even for dielectric systems, experimental artefacts due to residual absorption and inelastic scattering mar the data^{22,23,34–36}. Numerically, these artefacts can be excluded, but 3D random systems of sufficiently large dimension and large refractive index variation could not be simulated due to an extraordinarily long computational time required^{37,38}.

A recent implementation of the finite-difference time-domain (FDTD) algorithm on emerging computing hardware has brought orders of magnitude speed-up of numerical calculation^{39,40}. Using this highly efficient hardware-optimized version of the FDTD method, we solve the Maxwell equations by brute force in three dimensions. This enables us to simulate sufficiently large systems and large refractive index variation to address the following questions: can 3D AL of EM waves be achieved in fully random systems of dielectric scatterers? If not, can it occur in any other systems without the aid of spatial correlations?

Answering these long-standing questions not only addresses the fundamental aspects of wave transport and localization across multiple

¹Physics Department, Missouri University of Science and Technology, Rolla, MO, USA. ²Univ. Grenoble Alpes, CNRS, LPMMC, Grenoble, France.

³Flexcompute Inc, Belmont, MA, USA. ⁴Department of Electrical and Computer Engineering, University of Wisconsin, Madison, WI, USA. ⁵Department of Applied Physics, Yale University, New Haven, CT, USA. ✉e-mail: yamilov@mst.edu; zyu54@wisc.edu; hui.cao@yale.edu

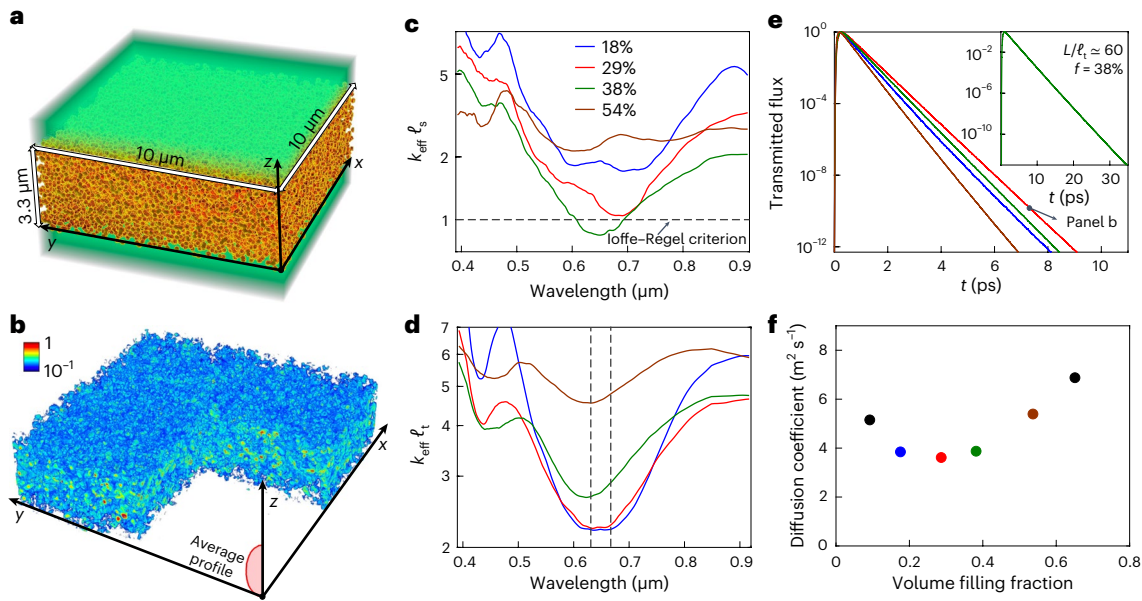


Fig. 1 | Absence of non-diffusive transport in random dielectric systems with a refractive index of 3.5. **a**, A 3D slab filled with dielectric spheres at random uncorrelated positions (radius $r = 100$ nm, refractive index $n = 3.5$) in air. The slab cross-section is $10 \mu\text{m} \times 10 \mu\text{m} = 100 \mu\text{m}^2$, and the thickness is $L = 3.3 \mu\text{m}$. **b**, The 3D distribution of light intensity inside the slab (dielectric filling fraction $f = 29\%$, $L/\ell_t = 33$) at long delay time after a short pulse of plane wavefront is incident on the front surface. The red curve with shading shows the average depth profile. **c**, The spectral dependence of the Ioffe–Regel parameter $k_{\text{eff}}\ell_s$ for different volume filling fractions of dielectric spheres, showing enhancement of scattering around single-sphere Mie resonances. The horizontal dashed line marks the

Ioffe–Regel criterion $k_{\text{eff}}\ell_s = 1$ for 3D localization. **d**, The transport mean free path ℓ_t (in units of $1/k_{\text{eff}}$) as a function of wavelength, revealing a saturation by dependent scattering at high dielectric filling fractions. The vertical dashed lines mark the spectral width (33 nm) of the excitation pulse in **b** and **e**. **e**, Transmittance of the 3D slab for a pulsed excitation, showing exponential decay in time for all dielectric filling fractions, in agreement with diffusive transport. The inset shows persistence of diffusion when L/ℓ_t is increased from 33 to 60 for $f = 38\%$ (green line). **f**, The dependence of the minimum diffusion coefficient within the pulse bandwidth on the dielectric filling fraction f , exhibiting a minimum value of $3.6 \text{ m}^2 \text{ s}^{-1}$ at $f \approx 30\%$.

disciplines but also opens new avenues in research and applications. For example, in topological photonics⁴¹, the interplay between disorder and topological phenomena may be explored beyond the limit of weak disorder in low-dimensional systems⁴². Also in cavity quantum electrodynamics with Anderson-localized modes⁴³, achieving 3D localization would avoid the out-of-plane loss inherent to two-dimensional (2D) systems and cover the full angular range of propagation directions⁴⁴. In addition to fundamental studies, disorder and scattering has been harnessed for various photonic device applications, but mostly with diffuse waves⁴⁵. Anderson-localized modes can be used for 3D energy confinement to enhance optical non-linearities and light–matter interactions, and to control random lasing as well as targeted energy deposition.

We first consider EM wave propagation through a 3D slab of randomly packed lossless dielectric spheres of radius $r = 100$ nm and refractive index $n = 3.5$ in air. This corresponds to the highest index difference achieved experimentally in the optical wavelength range with porous GaP around the wavelength of $\lambda = 650$ nm in the vicinity of the first Mie resonance of an isolated sphere (Supplementary Fig. S5). To avoid spatial correlations, the sphere positions are chosen completely randomly, leading to spatial overlap where the index is capped at the same value of n . We compute the spatial correlation function of such structure, which reveals that the correlation vanishes beyond the particle diameter (Supplementary Fig. S4). To avoid light reflection at the interfaces of the slab, we surround it by a uniform medium with a refractive index equal to the effective index of the slab, $n_{\text{eff}} = [(1-f) + fn^2]^{1/2}$, for a given dielectric volume filling fraction f (Fig. 1a). As described in Supplementary Sect. 1.5, for each wavelength, we compute the scattering mean free path ℓ_s directly from the rate of attenuation of co-polarized field with depth. This, together with the effective wavenumber $k_{\text{eff}} = n_{\text{eff}}(2\pi/\lambda)$, gives the Ioffe–Regel parameter

(Fig. 1c). It features a minimum at around $\lambda = 650$ nm and the smallest value of $k_{\text{eff}}\ell_s \approx 0.9$ is reached at $f = 38\%$. We also compute the transport mean free path ℓ_t from the continuous wave (CW) transmittance of an optically thick slab with thickness $L \gg \ell_t$ (Supplementary Sect. 1.7). In Fig. 1d, $k_{\text{eff}}\ell_t$ also exhibits a dip in the same wavelength range as $k_{\text{eff}}\ell_s$, but the smallest $k_{\text{eff}}\ell_t$ is found at lower f of 18–29%, as the dependent scattering sets in at higher f . In search for AL in this wavelength range, we numerically simulate the propagation of a narrowband Gaussian pulse centred at $\lambda_0 = 650$ nm with planar wavefront and compute the transmittance through the slab $T(t)$ as a function of arrival time t . The diffusive propagation time τ_D (approximately corresponds to the arrival time of the peak in Fig. 1e). At $t \gg \tau_D$, the decay of the transmitted flux is exponential over at least 12 orders of magnitude, as expected for purely diffusive systems⁴⁶. The rate of this exponential decay is $1/\tau_D$, which is directly related⁴⁶ to the smallest diffusion coefficient within the spectral range of the excitation pulse (Supplementary Sect. 1.8). In Fig. 1f, the dependence of this diffusion coefficient D on the dielectric filling fraction f exhibits a minimum at $f \approx 30\%$. Figure 1e (inset) shows that the further increase of the slab thickness does not lead to any deviation from diffusive transport. Furthermore, the diffusive behaviour persists in the numerical simulation with increased spatio-temporal resolution (Supplementary Sect. 1). At $t \gg \tau_D$, the spatial intensity distribution inside the system features a depth profile (averaged over cross-section) equal to that of the first eigenmode of the diffusion equation (Fig. 1b). We therefore rule out a possibility of AL in uncorrelated ensembles of dielectric spheres with $n = 3.5$.

At microwave frequencies, the refractive index may be even higher than $n = 3.5$. We therefore, perform numerical simulation of a 3D slab of dielectric spheres with $n = 10$. The main results are summarized here, and details are presented in Supplementary Sect. 2. A large scattering cross-section $\sigma_s(\lambda)$ of a single sphere near the first Mie resonance

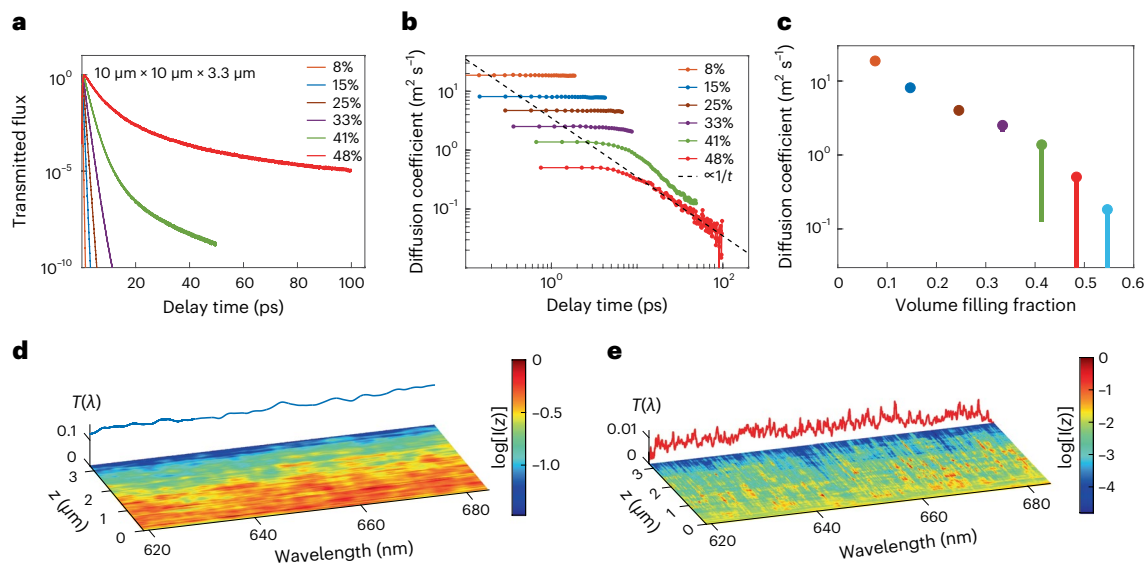


Fig. 2 | AL of light in 3D disordered PEC. **a**, The transmittance $T(t)$ of an optical pulse through a 3D slab ($10\ \mu\text{m} \times 10\ \mu\text{m} \times 3.3\ \mu\text{m}$) of randomly packed PEC spheres with radius $r = 50\ \text{nm}$ and volume filling fraction f from 8% to 48%. **b**, The time-resolved diffusion coefficient $D(t)$ extracted from the decay rate of $T(t)$ in **a**, decreasing with time as $1/t$ at high f . **c**, The short-time D (dots) and the interval of

variation of D with time (bars) at different f values. **d, e**, The CW transmittance spectrum $T(\lambda)$ in diffusive (**d**, $f = 15\%$, blue line) and localized (**e**, $f = 48\%$, red line) PEC slabs. Colour map: The depth profile of the average intensity $\langle I(x, y_0, z; \lambda) \rangle_x$ inside the slab at different wavelengths, highlighting the localized and necklace-like states for $f = 48\%$.

leads to strong dependent scattering even at small filling fractions. We find the Ioffe–Regel parameter $k_{\text{eff}}\ell_s \geq 1$ despite the very large refractive index difference. This is attributed to dependent scattering that becomes appreciable even at relatively low dielectric filling fraction f . The numerically calculated $T(t)$ for $L/\ell_t \gg 1$ does not exhibit any deviation from diffusive transport: at $t \gg \tau_D$, the decay of transmittance is still exponential over approximately ten orders of magnitude. In addition, scaling of CW transmittance with the inverse slab thickness $1/L$ remains linear for all f , as expected for diffusion (Supplementary Sect. 2). We therefore conclude that AL does not occur in random ensembles of dielectric spheres, thus closing the debate about the possibility of light localization in white paint^{8,23}.

Previous studies^{26,27} suggest that absence of AL for EM waves may be due to longitudinal waves that exist in a heterogeneous dielectric medium, where the transversality condition $\nabla \cdot \mathbf{E}(\mathbf{r}) = 0$ for the electric field $\mathbf{E}(\mathbf{r})$ does not follow from Gauss's law $\nabla \cdot [\epsilon(\mathbf{r})\mathbf{E}(\mathbf{r})] = 0$ because of the position dependence of $\epsilon(\mathbf{r})$. Here, we propose to suppress the contribution of longitudinal waves to optical transport and realize AL of EM waves by using perfectly conducting spheres as scatterers. The Poynting vector is parallel to the surface of a perfect electric conductor (PEC)⁴⁷, and EM energy flows around a PEC particle without coupling to longitudinal surface modes. The volume of PEC spheres is simply excluded from the free space and becomes unavailable for light. Thus, at high PEC volume fraction, light propagates in a random network of irregular air cavities and waveguides formed by the overlapping PEC spheres, akin to the original proposal of Anderson⁸.

Similarly to the dielectric systems above, we simulate a 3D slab composed of randomly packed, overlapping PEC spheres of radius $r = 50\ \text{nm}$ in air. Figure 2 shows the results of simulating an optical pulse propagating through $10\ \mu\text{m} \times 10\ \mu\text{m} \times 3.3\ \mu\text{m}$ slabs of various PEC volume fractions f . $T(t)$ displays non-exponential tails at high $f = 41\%$ or 48% in Fig. 2a. From the decay rate obtained via a sliding-window fit, we extract a time-dependent diffusion coefficient $D(t)$ (Fig. 2b), which shows a power-law decay with time, as predicted by the self-consistent theory of localization⁴⁸. The non-exponential decay of $T(t)$ and the time dependence of D are the signatures of AL^{13,48}. In contrast, at lower PEC fractions of $f = 8\%$ or 15% , D remains constant in time. Figure 2c reveals

a transition from time-invariant D to time-dependent $D(t)$ at around $f = 33\%$, where $D(t)$ starts deviating from a constant. Using a Fourier transform, we compute the spectrally resolved transmittance $T(\lambda)$. Figure 2d,e contrasts the $T(\lambda)$ of diffusive and localized systems. The former features smooth, gradual variations with λ due to broad overlapping resonances, whereas the latter exhibits strong resonant structures consistent with the average mode spacing exceeding the linewidth of individual modes, in accordance with the Thouless criterion of localization, as the spectral narrowing of modes is intimately related to their spatial confinement^{3,9,49}. The colour maps in Fig. 2d,e show the spatial intensity distributions inside the systems, $\langle I(x, y_0, z; \lambda) \rangle_x$, averaged over x at a cross-section $y = y_0$. These two-dimensional maps contrast slow variation with z and λ in the diffusive system (Fig. 2d) to the sharp features due to spatially confined modes in the localized system (Fig. 2e). Furthermore, there exist ‘necklace’ states with multiple spatially separated intensity maxima, originally predicted for electrons in metals⁵⁰.

Insight into the mechanism behind AL in the random ensemble of PEC spheres can be gained from the wavelength dependence of the Ioffe–Regel parameter $k\ell_s$ (Supplementary Sects. 1.5 and 3). We compute it using a procedure similar to that applied in dielectrics. Even at the volume fraction of $f = 8\%$, ℓ_s is well below the prediction of the independent scattering approximation (ISA), owing to scattering resonances formed by two or more neighbouring PEC spheres (Supplementary Fig. S10). As shown in Fig. 3a, ℓ_s becomes essentially independent of wavelength in the range of size parameter kr of PEC spheres. Consequently, the Ioffe–Regel parameter acquires $1/\lambda$ dependence (Fig. 3b). It drops below the value of unity within the excitation pulse bandwidth $\lambda \approx 650 \pm 45\ \text{nm}$ for f between 25% and 33%, in agreement with Fig. 2. We further conduct a finite-size scaling study, after computing the dependence of the CW transmittance T on the slab thickness L (Supplementary Sect. 1.9). Figure 3c shows the logarithmic derivative $d \log(T)/d \log(L)$ as a function of $k\ell_s$. In the diffusive regime, Ohm's law $T \propto 1/L$ is expected, leading to a scaling power of -1 , as indeed confirmed for $k\ell_s > 1$. Around $k\ell_s \approx 1$, we see a departure from $1/L$ scaling of transmittance. The scaling theory of localization predicts a single-parameter scaling of the dimensionless conductance $g = TN$ (refs. 51,52). By estimating the number

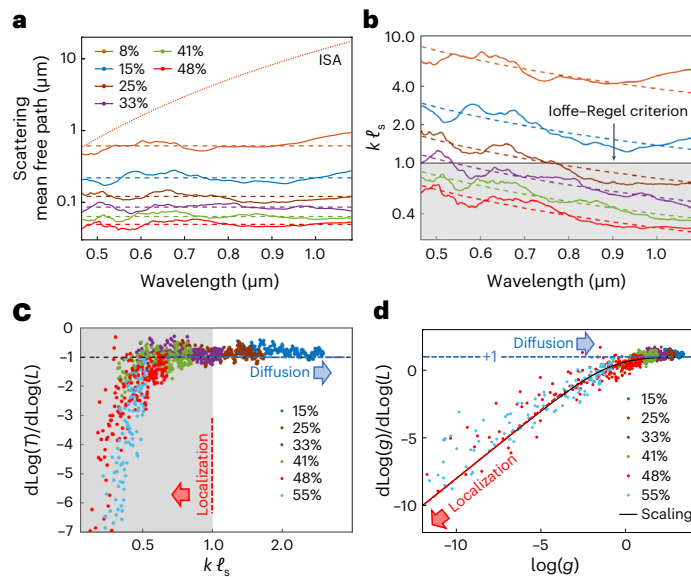


Fig. 3 | The transition from diffusion to AL in 3D disordered PEC. **a**, The scattering mean free path ℓ_s for PEC volume filling fraction f from 8% to 48%. ℓ_s is nearly flat (dashed lines) over a broad spectral range. **b**, The spectral dependence of the Ioffe–Regel parameter $k\ell_s$, exhibiting $1/\lambda$ dependence (dashed lines). **c**, The scaling of the CW transmittance T with the slab thickness L versus the Ioffe–Regel parameter $k\ell_s$, revealing a diffusion–localization transition at $k\ell_s \approx 1$. The dashed black line denotes diffusive scaling $T \propto L^{-1}$. The dashed red line marks $k\ell_s = 1$. The $k\ell_s < 1$ regime is highlighted as a shaded area in **b** and **c**. **d**, The single-parameter scaling of the dimensionless conductance g for the diffusion–localization transition (solid black line), in agreement with numerical data for six PEC filling fractions. Blue and red dashed lines denote diffusive and localized scalings $g \propto L$ and $g \propto \exp(-L/\xi)$, respectively, where ξ is the localization length.

of transverse modes as $N = 2\pi(L/\lambda)^2(1-f)^{2/3}$ for $L \times L$ area of the slab, we compute g and $\beta(g) \equiv d \log(g)/d \log(L)$. Figure 3d shows good agreement between the numerical data and the model function $\beta(g) = 2 - (1+g) \log(1+g^{-1})$ (ref. 52). In diffusive regime $g > 1$, $\beta(g) \rightarrow 1$. Meanwhile, in the localized regime $g < 1$, $\beta(g) \propto \log(g)$. The latter is a manifestation of the negative exponential scaling of g with L in the regime of AL.

To obtain the ultimate confirmation of AL of light in PEC composites, we simulate the dynamics of the transverse spreading of a tightly focused pulse—a measurement that has been widely adopted in localization experiments^{13,33,53}. A pulse centred at $\lambda = 650$ nm with a bandwidth of 90 nm is focused to a small spot of area approximately $0.5 \mu\text{m}^2$ at the front surface of a wide 3D slab of dimensions $33 \mu\text{m} \times 33 \mu\text{m} \times 3.3 \mu\text{m}$ (Fig. 4a). We compute the transverse extent of the intensity distribution $I(x, y, z = L; t)$ at the back surface of the slab. For a diffusive PEC slab with $f = 15\%$, we detect a rapid transverse spreading of light with time in Fig. 4b, which approaches the lateral boundary of the slab within approximately 2 ps. In sharp contrast, in the localized system in Fig. 4c ($f = 48\%$), the transmitted intensity profile remains transversely confined even after 20 ps. This time corresponds to a free space propagation of 6 mm, which is approximately 2,000 times longer than the actual thickness of the slab. Figure 4d quantifies this time evolution with the output beam diameter $d(t) = 2[\text{PR}(t)/\pi]^{1/2}$, where $\text{PR}(t) = [\iint I(x, y, L; t) dx dy]^2 / \iint I(x, y, L; t)^2 dx dy$ is the intensity participation ratio. For a diffusive slab, $d(t) \propto t^{1/2}$, while in the localized regime, $d(t)$ saturates at a value on the order of the slab thickness L . Such an arrest of the transverse spreading in the localized PEC systems persists with increased spatio-temporal resolution of the numerical simulation (Supplementary Sect. 1.3). Further evidence of AL includes non-linear decaying depth profile and strong non-Gaussian

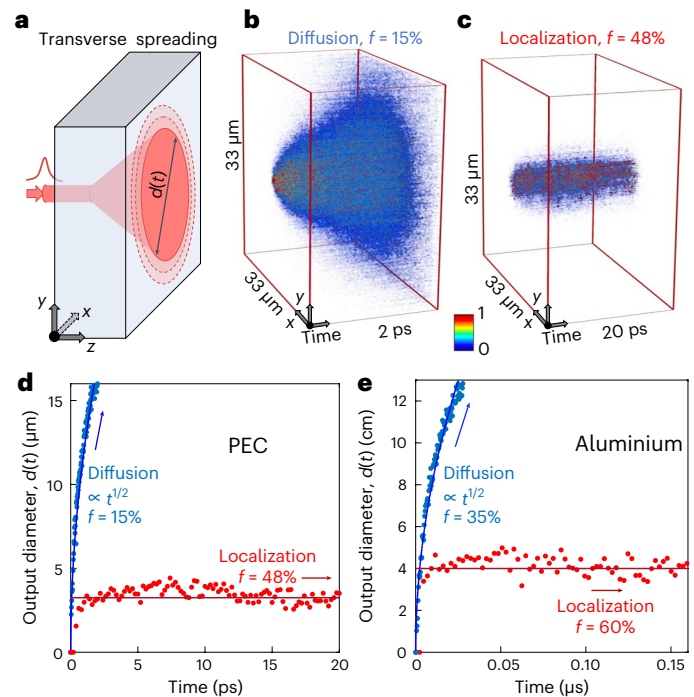


Fig. 4 | Arrest of transverse spreading of transmitted beam in 3D localized PEC systems. **a**, Schematic of transverse spreading of a tightly focused pulse propagating through a diffusive slab of cross-section $33 \mu\text{m} \times 33 \mu\text{m}$ and thickness $L = 3.3 \mu\text{m}$. **b**, The 2D intensity distribution at the output surface (normalized to the maximum, see colour bar) for different delay times, showing the lateral expansion of the beam in the diffusive slab with PEC filling fraction of $f = 15\%$. **c**, The absence of transverse spreading for $f = 48\%$, owing to AL. **d**, The lateral diameter of the transmitted beam $d(t)$ increases as \sqrt{t} (blue line) in the diffusive slab (blue dots) but saturates to a constant value (red line) in the localized slab (red dots). **e**, The same as **d** but for a slab ($L = 6$ cm) of aluminium spheres ($r = 0.28$ cm, $f = 35\%$ and 60%) with a realistic conductivity value of $\sigma_0 = 3.8 \times 10^4 \Omega^{-1} \text{m}^{-1}$ at a microwave frequency of approximately 20 GHz.

fluctuations of intensity inside the system (Supplementary Sect. 4.2). We also confirm our results by repeating calculations for 3D slabs of PEC spheres with larger radius $r = 100$ nm, obtaining similar scaling behaviour (Supplementary Sect. 4.2) as in Fig. 3c,d.

The striking difference between light propagation in dense random ensembles of dielectric and PEC spheres cannot be accounted for by the Ioffe–Regel parameter as both reach $k_{\text{eff}}\ell_s \approx 1$ for similar values of the size parameter kr (Figs. 1c and 3b). AL in 3D PEC composites with uncorrelated disorder reveals a localization mechanism that is unique to metal. In contrast to a dielectric system where light propagates everywhere (both inside and outside the scatterers), the propagation is restricted to the voids between scatterers in the PEC system. This makes AL inevitable when the wavelength becomes larger than the typical width of free-space channels between voids and light can hardly ‘squeeze’ through the latter to propagate from one void to another. This qualitative picture correctly predicts the increase of the critical volume fraction f for localization with the scatterer size r (Supplementary Sect. 3).

Finally, we test AL in real-metal aggregates. In the microwave spectral region, the skin depth of crystalline metals such as silver, aluminium and copper is several orders of magnitude shorter than the wavelength λ and the scatterer size r in the regime of $kr \approx 1$. Since the microwave barely penetrates into the metallic scatterers, our simulation results are almost identical to those for PEC. To account for the imperfections due to polycrystallinity, surface defects, oxide layers, etc., we lower the metal conductivity to match the experimentally measured

absorption rate in aggregates of aluminium spheres²⁹. Simulations unambiguously show the arrest of transverse spreading of a focused pulse (Fig. 4e), revealing AL in 3D random aggregates of aluminium spheres. Additional evidence of AL is presented in Supplementary Sect. 4. Moreover, even at optical frequencies, where realistic metals deviate notably from PEC, the arrest of transverse spreading persists in 3D silver nanocomposites (Supplementary Sect. 5). Possible light localization in 3D nanoporous metals will have a profound impact on their applications in photo-catalysis, optical sensing, and energy conversion and storage.

In summary, our large-scale microscopic simulations of EM wave propagation in 3D uncorrelated random ensembles of particles show no signs of AL for dielectric particles with refractive indices $n = 3.5$ – 10 . This explains multiple failed attempts of experimental observation of AL of light in 3D dielectric systems over the last three decades^{22,23,31–33}. At the same time, we report the first numerical evidence of EM wave localization in random ensembles of metallic particles over a broad spectral range. Localization is confirmed by eight criteria: the Ioffe–Regel criterion, the Thouless criterion, non-exponential decay of transmittance under pulsed excitation, vanishing of the diffusion coefficient, existence of spatially localized states, scaling of conductance, arrest of the transverse spreading of a narrow beam and enhanced non-Gaussian fluctuations of intensity. Our study calls for renewed experimental efforts to be directed at low-loss metallic random systems²⁹. In Supplementary Sect. 5.1, we propose a realistic microwave experiment that avoids experimental pitfalls and provides a tell-tale sign of AL.

Online content

Any methods, additional references, Nature Portfolio reporting summaries, source data, extended data, supplementary information, acknowledgements, peer review information; details of author contributions and competing interests; and statements of data and code availability are available at <https://doi.org/10.1038/s41567-023-02091-7>.

References

- Anderson, P. W. Absence of diffusion in certain random lattices. *Phys. Rev.* **109**, 1492–1505 (1958).
- Mott, N. Electrons in disordered structures. *Adv. Phys.* **16**, 49–144 (1967).
- Kramer, B. & MacKinnon, A. Localization: theory and experiment. *Rep. Prog. Phys.* **56**, 1469–1564 (1993).
- Imada, M., Fujimori, A. & Tokura, Y. Metal–insulator transitions. *Rev. Mod. Phys.* **70**, 1039–1263 (1998).
- Billy, J. et al. Direct observation of Anderson localization of matter waves in a controlled disorder. *Nature* **453**, 891–894 (2008).
- Jendrzejewski, F. et al. Three-dimensional localization of ultracold atoms in an optical disordered potential. *Nat. Phys.* **8**, 398–403 (2012).
- John, S. Electromagnetic absorption in a disordered medium near a photon mobility edge. *Phys. Rev. Lett.* **53**, 2169–2172 (1984).
- Anderson, P. W. The question of classical localization. A theory of white paint? *Philos. Mag. B* **52**, 505–509 (1985).
- Chabanov, A. A., Stoytchev, M. & Genack, A. Z. Statistical signatures of photon localization. *Nature* **404**, 850–853 (2000).
- Schwartz, T., Bartal, G., Fishman, S. & Segev, M. Transport and Anderson localization in disordered two-dimensional photonic lattices. *Nature* **446**, 52–55 (2007).
- Segev, M., Silberberg, Y. & Christodoulides, D. N. Anderson localization of light. *Nat. Photonics* **7**, 197–204 (2013).
- Kirkpatrick, T. R. Localization of acoustic waves. *Phys. Rev. B* **31**, 5746–5755 (1985).
- Hu, H., Strybulevych, A., Page, J. H., Skipetrov, S. E. & van Tiggelen, B. A. Localization of ultrasound in a three-dimensional elastic network. *Nat. Phys.* **4**, 945–948 (2008).
- Guazzelli, E., Guyon, E. & Souillard, B. On the localization of shallow water waves by random bottom. *J. Phys. Lett.* **44**, 837–841 (1983).
- Sheng, P., White, B., Zhang, Z. Q. & Papanicolaou, G. in *Scattering and Localization of Classical Waves in Random Media, Directions in Condensed Matter Physics* (ed. Sheng, P.) 563–619 (World Scientific, 1990).
- Rothstein, I. Z. Gravitational Anderson localization. *Phys. Rev. Lett.* **110**, 011601 (2013).
- John, S. Localization of light. *Phys. Today* **44**, 32–40 (1991).
- Sheng, P. *Introduction to Wave Scattering, Localization and Mesoscopic Phenomena* (Springer, 2006).
- Lagendijk, A., van Tiggelen, B. & Wiersma, D. S. Fifty years of Anderson localization. *Phys. Today* **62**, 24–29 (2009).
- Ioffe, A. F. & Regel, A. R. Non-crystalline, amorphous, and liquid electronic semiconductors. *Prog. Semicond.* **4**, 237–291 (1960).
- Haberko, J., Froufe-Perez, L. S. & Scheffold, F. Transition from light diffusion to localization in three-dimensional amorphous dielectric networks near the band edge. *Nat. Commun.* **11**, 4867 (2020).
- van der Beek, T., Barthelemy, P., Johnson, P. M., Wiersma, D. S. & Lagendijk, A. Light transport through disordered layers of dense gallium arsenide submicron particles. *Phys. Rev. B* **85**, 115401 (2012).
- Sperling, T. et al. Can 3D light localization be reached in ‘white paint’? *N. J. Phys.* **18**, 013039 (2016).
- Lahini, Y. et al. Anderson localization and nonlinearity in one-dimensional disordered photonic lattices. *Phys. Rev. Lett.* **100**, 013906 (2008).
- Skipetrov, S. E. & Page, J. H. Red light for Anderson localization. *N. J. Phys.* **18**, 021001 (2016).
- Skipetrov, S. E. & Sokolov, I. M. Absence of Anderson localization of light in a random ensemble of point scatterers. *Phys. Rev. Lett.* **112**, 023905 (2014).
- van Tiggelen, B. A. & Skipetrov, S. E. Longitudinal modes in diffusion and localization of light. *Phys. Rev. B* **103**, 174204 (2021).
- Cobus, L. A., Maret, G. & Aubry, A. Crossover from renormalized to conventional diffusion near the three-dimensional Anderson localization transition for light. *Phys. Rev. B* **106**, 014208 (2022).
- Genack, A. Z. & Garcia, N. Observation of photon localization in a three-dimensional disordered system. *Phys. Rev. Lett.* **66**, 2064–2067 (1991).
- Watson Jr, G., Fleury, P. & McCall, S. Searching for photon localization in the time domain. *Phys. Rev. Lett.* **58**, 945 (1987).
- Wiersma, D. S., Bartolini, P., Lagendijk, A. & Righini, R. Localization of light in a disordered medium. *Nature* **390**, 671–673 (1997).
- Störzer, M., Gross, P., Aegerter, C. M. & Maret, G. Observation of the critical regime near Anderson localization of light. *Phys. Rev. Lett.* **96**, 063904 (2006).
- Sperling, T., Bührer, W., Aegerter, C. M. & Maret, G. Direct determination of the transition to localization of light in three dimensions. *Nat. Photonics* **7**, 48–52 (2013).
- Scheffold, F., Lenke, R., Tweer, R. & Maret, G. Localization or classical diffusion of light? *Nature* **398**, 206–207 (1999).
- Wiersma, D. S., Rivas, J. G., Bartolini, P., Lagendijk, A. & Righini, R. Reply: Localization or classical diffusion of light? *Nature* **398**, 207–207 (1999).
- Scheffold, F. & Wiersma, D. Inelastic scattering puts in question recent claims of Anderson localization of light. *Nat. Photonics* **7**, 934 (2013).
- Gentilini, S., Fratilocchi, A., Angelani, L., Ruocco, G. & Conti, C. Ultrashort pulse propagation and the Anderson localization. *Opt. Lett.* **34**, 130–132 (2009).

38. Pattelli, L., Egel, A., Lemmer, U. & Wiersma, D. S. Role of packing density and spatial correlations in strongly scattering 3D systems. *Optica* **5**, 1037–1045 (2018).
39. *Flexcompute Inc.* <https://flexcompute.com> (2021).
40. Hughes, T. W., Minkov, M., Liu, V., Yu, Z. & Fan, S. A perspective on the pathway toward full wave simulation of large area metalenses. *Appl. Phys. Lett.* **119**, 150502 (2021).
41. Lu, L., Joannopoulos, J. D. & Soljacic, M. Topological photonics. *Nat. Photonics* **8**, 821–829 (2014).
42. Stützer, S. et al. Photonic topological Anderson insulators. *Nature* **560**, 461–465 (2018).
43. Sapienza, L. et al. Cavity quantum electrodynamics with Anderson-localized modes. *Science* **327**, 1352–1355 (2010).
44. Wiersma, D. S. Random quantum networks. *Science* **327**, 1333–1334 (2010).
45. Cao, H. & Eliezer, Y. Harnessing disorder for photonic device applications. *Appl. Phys. Rev.* **9**, 011309 (2022).
46. Akkermans, E. & Montambaux, G. *Mesoscopic Physics of Electrons and Photons* (Cambridge Univ. Press, 2007).
47. van de Hulst, H. C. *Light Scattering by Small Particles* (Dover, 1981).
48. Skipetrov, S. E. & van Tiggelen, B. A. Dynamics of Anderson localization in open 3D media. *Phys. Rev. Lett.* **96**, 043902 (2006).
49. Thouless, D. J. Electrons in disordered systems and the theory of localization. *Phys. Rep.* **13**, 93–142 (1974).
50. Pendry, J. B. Quasi-extended electron states in strongly disordered systems. *J. Phys. C* **20**, 733–742 (1987).
51. Abrahams, E., Anderson, P. W., Licciardello, D. C. & Ramakrishnan, T. V. Scaling theory of localization: absence of quantum diffusion in two dimensions. *Phys. Rev. Lett.* **42**, 673–676 (1979).
52. Müller, C. A. & Delande, D. In *Ultracold Gases and Quantum Information: Lecture Notes of the Les Houches Summer School in Singapore* (eds. Miniatura, C.) Chapter 9 (Oxford Univ. Press, 2011).
53. Cherroret, N., Skipetrov, S. E. & van Tiggelen, B. A. Transverse confinement of waves in three-dimensional random media. *Phys. Rev. E* **82**, 056603 (2010).

Publisher's note Springer Nature remains neutral with regard to jurisdictional claims in published maps and institutional affiliations.

Springer Nature or its licensor (e.g. a society or other partner) holds exclusive rights to this article under a publishing agreement with the author(s) or other rightsholder(s); author self-archiving of the accepted manuscript version of this article is solely governed by the terms of such publishing agreement and applicable law.

© The Author(s), under exclusive licence to Springer Nature Limited 2023

Data availability

Figures reported in this work, containing the source data, are available via download from https://scholarsmine.mst.edu/phys_facwork/2259/. All other data that support the findings of this study are available from the corresponding authors upon reasonable request. Source data are provided with this paper.

Code availability

The simulation project and associated codes can be found at <https://www.flexcompute.com/userprojects/anderson-localization-of-electromagnetic-waves-in-three-dimensions>. A Tidy3D software license can be requested from Flexcompute Inc to reproduce simulation results.

Acknowledgements

This work is supported by the National Science Foundation under grant nos. DMR-1905442 and DMR-1905465 and the Office of Naval Research (ONR) under grant no. N00014-20-1-2197. We thank S. Fan and B. van Tiggelen for enlightening discussions. A.Y. expresses gratitude to LPMCC (CNRS) for hospitality.

Author contributions

A.Y. performed numerical simulations, analysed the data and compiled all results. S.E.S. conducted theoretical study and guided data interpretation. T.W.H. and M.M. implemented the

hardware-accelerated FDTD method and aided in the setup of the numerical simulations. Z.Y. and H.C. initiated this project and supervised the research. A.Y. wrote the first draft, S.E.S. and H.C. revised the content and scope, and T.W.H., M.M. and Z.Y. edited the manuscript. All co-authors discussed and approved the content.

Competing interests

T.W.H., M.M. and Z.Y. have financial interest in Flexcompute Inc., which develops the software Tidy3D used in this work.

Additional information

Supplementary information The online version contains supplementary material available at <https://doi.org/10.1038/s41567-023-02091-7>.

Correspondence and requests for materials should be addressed to Alexey Yamilov, Zongfu Yu or Hui Cao.

Peer review information *Nature Physics* thanks Luis Froufe-Pérez, Diederik Wiersma and the other, anonymous, reviewer(s) for their contribution to the peer review of this work.

Reprints and permissions information is available at www.nature.com/reprints.

Supplementary Information: Anderson localization of electromagnetic waves in three dimensions

Alexey Yamilov^{1*}, Sergey E. Skipetrov², Tyler W. Hughes³, Momchil Minkov³,
Zongfu Yu^{4,†}, Hui Cao^{5*}

¹Physics Department, Missouri University of Science & Technology, Rolla, Missouri 65409

²Univ. Grenoble Alpes, CNRS, LPMMC, 38000 Grenoble, France

³Flexcompute Inc, 130 Trapelo Road, Belmont, MA, 02478

⁴Dept. of Electrical & Computer Engineering, University of Wisconsin, Madison, WI, 53705

⁵Department of Applied Physics, Yale University, New Haven, Connecticut 06520

* yamilov@mst.edu

† zyu54@wisc.edu

* hui.cao@yale.edu

1 Methods

1.1 Numerical method

Over the years, various techniques have been developed for large-scale 3D computations. One efficient method for simulating light scattering in large inhomogeneous media is based on Born series ($S1, S2$). This method, however, is limited to small difference in refractive index between the scatterers and the host medium. To achieve 3D localization, a large refractive-index difference is needed to enhance light scattering, which makes it necessary to include many terms of the Born series. This greatly increases the computational complexity, worsening the convergence of such an iterative algorithm.

Another family of approaches for simulating wave transport in 3D aggregates of spherical particles is based on iterative multi-sphere scattering expansions, e.g., the generalized multi-

particle-Mie (GMM) formalism (S3, S4, S5), the multi-sphere T-matrix (MSTM) (S6), and the fast multipole method (FMM) (S7). The latest, and the most advanced implementation, deployed on GPUs for speedup, is capable of simulating up to 10^5 dielectric spheres (S8), (38). However, the state-of-the-art algorithm (CELES) has not been used for index higher than 2 (in air). This is because the Mie resonances of high-index spheres can have very long lifetimes and strong internal fields, leading the algorithm to either converge extremely slowly or fail to converge. Moreover, the spheres cannot touch or overlap, which would invalidate the Mie solution for isolated spheres. If two spheres are very close to each other, the near-field effects will excite high-order multipoles, causing slow or failed convergence. Therefore, these methods require a minimum distance between densely-packed spheres, which introduces spatial correlations of the scattering structures (38) that are known to affect Anderson localization (S9), (21).

The finite-difference time-domain (FDTD) method directly solves the Maxwell's equations in space and time (S10). It does not make any physical approximations, and is capable of simulating large-refractive-index, spatially-overlapping or touching particles with high filling fraction. The effects of spatial correlations of scattering structures that could contribute to Anderson localization (S9), (21), are avoided by a completely random placement of individual scatterers in our study, as shown in Sec. 1.4 below.

The ability to simulate refractive-index of 3.5–10 (with air background) in our study is the key to assert that increasing index difference will not precipitate Anderson localization. However, simulating such high refractive-index particles requires very fine spatial and temporal resolution, leading to an extremely long computational time. Previous FDTD simulations were limited to small 3D structures containing 10^3 – 10^4 particles (37), (21). Our hardware-accelerated implementation of the FDTD method (39) reduces the computational time by several orders of magnitude, allowing us to simulate a 3D system with 6×10^6 scatterers in about 40 min.

The orders-of-magnitude reduction in computational time is essential to *search* for Ander-

son localization in 3D PEC and real-metal composites, because it allows one to repeat the simulations many times with varying parameters such as particle size, volume fraction, dielectric function and conductivity, lateral dimension and thickness of simulated systems, etc. Moreover, our time-domain simulation can extract the fields at more than 1000 discrete frequencies from a single run through a Fourier transform. In contrast, the frequency-domain methods based on Born series and GMM/MSTM simulate only one frequency per run. Using such methods to simulate time-dependent transport, particularly at long delay time, requires repeating the calculations at many closely-spaced frequencies so that the Fourier transform will give the long-time behavior.

1.2 System geometry and dimension

Unless otherwise specified, our simulations are carried out on disordered systems in the slab geometry $L_x = L_y \gg L$ (Fig. 1a). A plane wave with the electric field polarized along x -axis is incident on the front surface of the slab. The default bandwidth of a Gaussian pulse, $\Delta\lambda = 90$ nm, is chosen such that a Fourier transform can be reliably used in the desired spectral range. In the dynamic simulations of dielectrics, the bandwidth was reduced to $\Delta\lambda = 33$ nm [Fig. 1b,e, Fig. S2], or even to $\Delta\lambda = 11$ nm [Fig. S9], so that ℓ_t remains nearly invariant with wavelength. Periodic boundary conditions are applied along x and y axes. To ensure that the periodicity does not affect the results presented in this manuscript, we make the transverse dimensions L_x, L_y of the simulated slabs much larger than the thickness L . In the transmission simulations such as those in Fig. 1, the ratio is $L_x/L = L_y/L = 3$, so that any effect induced by periodic boundary conditions occurs on a length scale much larger than any relevant transport or localization scales. For the simulations of the transverse spreading (Figs. 4,S3,S20), we simulate much wider slabs having $L_x/L = L_y/L = 10$ to avoid any edge effect.

Figure number	Center wavelength λ_0	Simulation volume $L_x \times L_y \times \tilde{L}_z$	Number of spatial cells $N_x \times N_y \times N_z$	Simulated time interval	Total time steps
Fig. 1c,d	0.55 μm	$55 \times 1.1 \times 5.5 \mu\text{m}^3$	$2000 \times 40 \times 200$	1 ps	0.2×10^5
Fig. 1e,f	0.65 μm	$9.75 \times 9.75 \times 8.45 \mu\text{m}^3$	$300 \times 300 \times 260$	up to 30 ps	5×10^5
Fig. 2a-c	0.65 μm	$9.75 \times 9.75 \times 8.45 \mu\text{m}^3$	$300 \times 300 \times 260$	up to 100 ps	1.8×10^6
Fig. 2d,e	0.65 μm	$9.75 \times 9.75 \times 8.45 \mu\text{m}^3$	$300 \times 300 \times 260$	10 ps	1.8×10^5
Fig. 3a,b	0.65 μm	$65 \times 1.3 \times 6.5 \mu\text{m}^3$	$2000 \times 40 \times 200$	up to 7 ps	1.2×10^5
Fig. 3c,d	0.65 μm	$3.9 \times 3.9 \times 6.5 \mu\text{m}^3$	$120 \times 120 \times 200$	up to 10 ps	1.8×10^5
		$9.75 \times 9.75 \times 8.45 \mu\text{m}^3$	$300 \times 300 \times 260$	up to 100 ps	1.8×10^6
Fig. 4b-d	0.65 μm	$32.5 \times 32.5 \times 8.45 \mu\text{m}^3$	$1000 \times 1000 \times 260$	up to 20 ps	3.6×10^5
Fig. 4e	1.5 cm	$60 \times 60 \times 18 \text{cm}^3$	$800 \times 800 \times 240$	up to 0.16 μs	1.2×10^5
Fig. S2	0.65 μm	$9.75 \times 9.75 \times 8.45 \mu\text{m}^3$	$600 \times 600 \times 520$	9 ps	3.2×10^5
Fig. S3	0.65 μm	$13 \times 13 \times 6.5 \mu\text{m}^3$	$800 \times 800 \times 400$	up to 2 ps	0.7×10^5
Fig. S5	0.65 μm	$65 \times 1.3 \times 6.5 \mu\text{m}^3$	$2000 \times 40 \times 200$	up to 7 ps	1.2×10^5
Fig. S6	0.65 μm	$16.25 \times 0.65 \times 3.25 \mu\text{m}^3$	$1500 \times 60 \times 300$	up to 2 ps	1.1×10^5
Fig. S7	0.65 μm	$65 \times 1.3 \times 6.5 \mu\text{m}^3$	$2000 \times 40 \times 200$	up to 7 ps	1.2×10^5
Fig. S8	0.65 μm	$65 \times 1.3 \times 6.5 \mu\text{m}^3$	$2000 \times 40 \times 200$	up to 7 ps	1.2×10^5
Fig. S9b,c	0.65 μm	$16.25 \times 0.65 \times 3.25 \mu\text{m}^3$	$1500 \times 60 \times 300$	up to 2 ps	1.1×10^5
Fig. S9d	0.65 μm	$1.95 \times 1.95 \times 5.2 \mu\text{m}^3$	$180 \times 180 \times 480$	up to 25 ps	1.3×10^6
Fig. S9e	0.65 μm	$3.25 \times 3.25 \times 3.9 \mu\text{m}^3$	$300 \times 300 \times 360$	up to 35 ps	1.9×10^6
Fig. S11	0.65 μm	$9.75 \times 9.75 \times 8.45 \mu\text{m}^3$	$300 \times 300 \times 260$	10 ps	1.8×10^5
Fig. S12	0.65 μm	$9.75 \times 9.75 \times 8.45 \mu\text{m}^3$	$300 \times 300 \times 260$	25 ps	4.4×10^5
Fig. S13	0.65 μm	$9.75 \times 9.75 \times 8.45 \mu\text{m}^3$	$300 \times 300 \times 260$	up to 100 ps	1.8×10^6
Fig. S14	0.65 μm	$9.75 \times 9.75 \times 8.45 \mu\text{m}^3$	$300 \times 300 \times 260$	up to 100 ps	1.8×10^6
Fig. S15	0.65 μm	$9.75 \times 9.75 \times 8.45 \mu\text{m}^3$	$300 \times 300 \times 260$	10 ps	1.8×10^5
Fig. S16	0.65 μm	$9.75 \times 9.75 \times 8.45 \mu\text{m}^3$	$300 \times 300 \times 260$	up to 100 ps	1.8×10^6
Fig. S17	0.65 μm	$3.9 \times 3.9 \times 6.5 \mu\text{m}^3$	$120 \times 120 \times 200$	up to 10 ps	1.8×10^5
	0.65 μm	$9.75 \times 9.75 \times 8.45 \mu\text{m}^3$	$300 \times 300 \times 260$	up to 50 ps	0.9×10^6
Fig. S19	1.5 cm	$15 \times 15 \times 18 \text{cm}^3$	$200 \times 200 \times 240$	up to 0.23 μs	1.8×10^5
Fig. S20	0.65 μm	$19.5 \times 19.5 \times 7.15 \mu\text{m}^3$	$600 \times 600 \times 220$	up to 1.8 ps	0.3×10^5

Table 1: **Parameters of numerical simulations.** The table lists space and time domain parameters for simulations reported in all figures of the main text and supplementary information. \tilde{L}_z is the overall z -dimension of the system including the slab, two boundary layers (perfect matching layer - PML) and air-buffers in between.

The slab is sandwiched between homogeneous layers of refractive index n_B and thickness Δ_B , which in turn are surrounded by perfectly matched layers of thickness Δ_{PML} . These thicknesses are chosen as $\Delta_B = \Delta_{PML} = 2\lambda_0, \lambda_0, 2\lambda_0$ for the slabs of dielectric spheres with refractive index $n = 3.5, 10$ and PEC spheres, respectively. For the dielectric slabs, n_B is equal to the effective index n_{eff} found by averaging the dielectric constant, while for PEC $n_B = 1$. $\lambda_0 = 650 \text{ nm}$ is the central wavelength of optical pulses in all simulations. The spatial

discretization step of the FDTD algorithm is $\lambda_0/20$ for $n = 3.5$ and PEC, and $\lambda_0/60$ for $n = 10$. This corresponds to time steps of $dt \simeq 56 \times 10^{-18}$ s and $dt \simeq 19 \times 10^{-18}$ s, respectively. Table 1 lists parameters for numerical simulations of results presented in all figures. The FDTD time stepping for a single simulation with e.g. a total domain size of $15\lambda \times 15\lambda \times 9\lambda$ and run time of 10 ps took two minutes on an elastic network instance with 8 A100 GPUs.

To reproduce our numerical results, one needs to specify the proper volume filling fraction of the disordered structure to be simulated. The nominal filling fraction $f_{nominal} = N_{sph} [4\pi r^3/3]/V$, given by the number of spheres N_{sph} in volume V , differs from the actual filling fraction f due to the following factors:

- (i) spatial overlap caused by random placement of spheres;
- (ii) discretization effects due to how material properties are assigned on the spatial grids;
- (iii) internal averaging/smoothing procedure employed to improve accuracy and/or convergence of the algorithm.

The effect of sphere overlap in (i) can be accounted for theoretically (S11) as $\tilde{f} = 1 - \exp[-f_{nominal}]$. However, $\tilde{f} \neq f$, and quantifying the remaining effect due to (ii-iii) is less obvious. To make the process of structure generation more straightforward, we create the mapping in Fig. S1. For each type of structure simulated in this work, it allows one to determine $f_{nominal}$ from f , and then N_{sph} . Subsequently, the desired random structure can be generated by placing N_{sph} spheres completely randomly throughout volume V .

1.3 Numerical accuracy and scaling

Tidy3D solver (39) is an implementation of the standard FDTD method, which does not make any physical approximations or impose any constraint on the scattering structures. To accomplish accurate numerical modelling in FDTD, one must be sure to set a sufficiently fine discretization of space and time (S10). To this end, we have carefully tested spatio-temporal reso-

lution of FDTD simulations to ensure consistency of our numerical results through conversion studies, so that the conclusions of our study are robust and independent of the discretization. We present two examples of such tests below.

(i) One key evidence for the absence of AL in 3D dielectric random media is the exponential decay of transmitted flux $T(t)$, shown in Fig. 1e of the main text. This result is obtained with the spatial grid size of $\lambda_0/20$. When the spatial grid is reduced to $\lambda_0/40$ and the temporal step size is also halved, the exponential decay of $T(t)$ persists over 12 orders of magnitude in Fig. S2, which confirms the diffusive transport. (ii) A tell-tale sign of AL in PEC composites is the arrest of transverse spreading of the transmitted beam when an incident pulse is focused on a slab, as shown in Fig. 4c,d of the main text. This result is obtained with numerical resolution of $\lambda_0/20$. To test the robustness of this result, we vary the resolution from $\lambda_0/10$ to $\lambda_0/40$. Fig. S3a shows the result with $\lambda_0/40$ resolution: the transverse diameter of transmitted beam $d(t)$ saturates to a constant value in time, consistent with the result of $\lambda_0/20$ resolution in Fig. 4d. The asymptotic beam diameter d_∞ is plotted versus the numerical resolution in Fig. S3b. It confirms the consistency of our numerical results: the arrest of transverse spreading persists in all simulations performed on the progressively finer meshes. Notably, the arrest is already seen in simulations with $\lambda_0/10$ resolution, despite a slight difference in the value of d_∞ .

Since Tidy3D implements the standard FDTD algorithm, the scaling of computing time with system size is the same as the standard FDTD method (S10). More specifically, the computing time scales as $N_x N_y N_z N_t$, where N_x, N_y, N_z denote the number of spatial grid points in x, y, z dimensions and N_t is the total number of time steps. Typically the spatial grid size along x, y, z is identical, and it is proportional to the time step.

We note that the finite difference discretization introduces slight anisotropy and dispersion to the simulated system. To mitigate such effects, the spatio-temporal resolution could be further increased according to the system size, which would affect the scaling of computing time (S2).

However, this is not necessary in our simulations of random ensembles of dielectric or metal spheres because the statistical properties, like scattering and transport mean free paths, are barely modified. By varying the spatio-temporal grid size, we find the small effects caused by finite discretization are simply equivalent to a minuscule change of the refractive index n of the medium and/or a minuscule change of the volume filling fraction f . As shown in the manuscript, AL is absent in the dielectric systems for a broad range of n 's, whereas AL persists in a broad range of f 's in the metallic systems, so these small changes in n and f have negligible effects on the results.

Our extensive tests of the numerical procedure and accuracy confirm the consistency and robustness of the results and conclusions in this manuscript.

1.4 Spatial correlation function

In order to avoid any residual spatial correlation of the scattering structures, we adopt a uniform random distribution of scatterer centers. The structure factor obtained from a Fourier transform of center positions is equal to unity ($S12$). The spheres with center spacing smaller than their diameter will overlap in space, and the overlapping region is assigned the refractive index equal to that of an isolated sphere.

We calculate the spatial correlation function $C(\Delta) = \langle h(\boldsymbol{\rho}) h(\boldsymbol{\rho} + \boldsymbol{\Delta}) \rangle / \langle h(\boldsymbol{\rho}) \rangle^2 - 1$, where, $\boldsymbol{\rho}$ denotes the spatial position, $h(\boldsymbol{\rho})$ is a binary function equal to 1 inside the dielectric/PEC/metal scatterers and 0 outside, and $\langle \dots \rangle$ denotes averaging over $\boldsymbol{\rho}$, direction of $\boldsymbol{\Delta}$, and random ensemble. Fig. S4 shows the normalized $C(\Delta)/C(0)$ with $h(\boldsymbol{\rho})$ obtained from the discretized structures in the actual FDTD calculations of systems with particle radii $r = 50$ nm and 100 nm, and the PEC volume fractions of $f \sim 15\%$ and $\sim 50\%$. In all cases, the spatial correlation vanishes beyond the range Δ of one particle diameter $2r$, as expected for a random arrangement of spherical particles.

1.5 Scattering mean free path

The scattering mean free path ℓ_s measures the average distance traveled between two consecutive scattering events. Its value in Figs. 1c and 3a is extracted from the attenuation of the coherent component of the incident field. We simulate systems with dimension $L_x = 100\lambda_0, L_y = L = 2\lambda_0$ for an $n = 3.5$ dielectric and PEC, $L_x = 25\lambda_0, L_y = L = \lambda_0$ in the $n = 10$ dielectric. The quantity $\langle E_x(x, y_0, z; \lambda) \rangle_x$ is computed by averaging over the long dimension (along x -axis) of the system for one particular cross-section $y = y_0$. The average of the co-polarized field amplitude $|\langle E_x(x, y_0, z; \lambda) \rangle_x|$ decays exponentially with z at a rate $1/(2\ell_s)$, from which ℓ_s is obtained for each wavelength. The phase of $\langle E_x(x, y_0, z; \lambda) \rangle_x$ gives k_{eff} .

Figures S5, S6, S7 show the amplitude and phase of the coherent field $\langle E_x(x, y_0, z; \lambda) \rangle_x$, as well as its real and imaginary parts, in random aggregates of dielectric spheres and PEC spheres. In the dielectric systems, spectral regions with strong attenuation, i.e. short scattering mean free path, are concentrated in the vicinity of the Mie resonances of the constituent spherical particles. In contrast, in the PEC systems, the scattering mean free path does not exhibit notable spectral features in Fig. 3a. In Figs. S7a,e, this can be seen from a constant attenuation rate of the field amplitude.

1.6 Effective wavenumber

We extract k_{eff} from the average co-polarized coherent field $\bar{E}_x(z; \lambda) = \langle E_x(x, 0, z; \lambda) \rangle_x$ in Figs. S5, S6, S7. First, we obtain its phase ϕ , normalized by vacuum wavenumber $k = 2\pi/\lambda$ and average over the entire wavelength range of simulation for the PECs or the $\lambda > 650$ nm wavelength range for dielectrics. $\phi(z)$ increases linearly with depth z near the front surface of the slab, as shown in Fig. S8. The slope gives k_{eff}/k . For the disordered dielectric slab, the slope is close to the effective index of refraction $n_{\text{eff}} = [(1 - f) + fn^2]^{1/2}$, where $n = 3.5$ is the refractive index of overlapping dielectric spheres ($r = 100$ nm), and f is the dielectric filling

fraction. For the PEC slabs with overlapping spheres of $r = 50$ nm and 100 nm, the slopes are approximately equal to unity, even at high filling fraction $f \simeq 50\%$, c. f. Fig. S8. This justifies that we use the vacuum k to approximate k_{eff} in the Ioffe-Regel criterion for disordered PEC systems.

1.7 Transport mean free path

Transport mean free path ℓ_t corresponds to the average travel distance that is required to completely randomize the propagation direction. Transmittance of a continuous wave (CW) at wavelength λ through a diffusive slab of thickness L is $T(\lambda) = (5/3)\ell_t(\lambda)/[L + 2z_0(\lambda)]$, where $z_0(\lambda)$ is the extrapolation length (46). The value of $z_0(\lambda)$ can be estimated from the CW depth profile of the internal intensity $I(z, \lambda)$ by linear extrapolation $I(z = L + z_0, \lambda) = 0$ (Fig. S14b). Then the value of $\ell_t(\lambda)$ can be extracted from $T(\lambda)$ with known $z_0(\lambda)$.

Typically, z_0 depends on the refractive-index mismatch between the slab and the surrounding medium (46). However, our choice of refractive index n_{eff} for the surrounding layers eliminates this mismatch for a dielectric slab, leading to $z_0 = (2/3)\ell_t$ (46). Our numerical data suggest that this relation approximately holds for PEC composites embedded in air as well.

1.8 Diffusion coefficient

The diffusion coefficient $D = \ell_t v_E / 3$ depends on both the transport mean free path ℓ_t and the energy transport velocity v_E (S13). The propagation of an optical pulse in a slab geometry makes it possible to directly extract D from the decay of the transmittance, $T(t) \propto \exp[-t/t_D]$, where $1/t_D = \pi^2 D / (L + 2z_0)^2$. In the localized slabs such as those in Fig. 2, the decay rate, $1/t_D$, changes with time. To obtain $D(t)$ in Fig. 2b, we use an exponential fit within a time window $[t - 2\tau_D, t + 2\tau_D]$, where τ_D is the arrival time of the peak of transmitted flux.

1.9 Scaling functions

To obtain the scaling function $d \log(T)/d \log(L)$ for the PEC slabs, we compute the logarithmic derivative of CW transmittance T with respect to slab thickness L for a range of values of $k\ell_s$. First, we use the wavelength dependence of $k\ell_s$ in Fig. 3a to map $k\ell_s$ to λ for each f . Next, we compute $T(\lambda)$ for two systems with different thicknesses $L_1 = 2\lambda_0$ and $L_2 = 5\lambda_0$, where $\lambda_0 = 650$ nm denotes the center of the wavelength range of interest. Finally, we approximate $d \log(T)/d \log(L)$ by the finite difference $[\log(T_2) - \log(T_1)]/[\log(L_2) - \log(L_1)]$ for all λ and all f . After eliminating λ , we obtain the dependence of $d \log(T)/d \log(L)$ on the Ioffe-Regel parameter $k\ell_s$ shown in Fig. 3c.

The same procedure is used to obtain the scaling of conductance g in Figs. 3d and S17b. We calculate the conductance of a $L \times L \times L$ cube as a product of the transmission T of a slab of thickness L (computed in our simulations) and the number of transverse channels N in the $L \times L$ cross-section of the cube. We estimate that $N = 2\pi(L/\lambda)^2(1 - f)^{2/3}$, where the $(1 - f)^{2/3}$ factor accounts for the presence of PEC. The conductance g , calculated in this way, is equal to the Thouless conductance up to a prefactor of order 1.

2 Absence of light localization in 3D dielectric systems with refractive-index of 10

This section reports numerical simulations of 3D slab of dielectric spheres with $n = 10$. For ease of comparison, we adjust the sphere radius to $r = 32$ nm, so that the first Mie resonance occurs at a wavelength similar to that of a single $n = 3.5$ sphere (compare Figs S5a and S6a). Scattering cross-section of a single sphere of $n = 10$ is exceedingly large (Fig. S9a), leading to strong dependent scattering already at small volume filling fractions, and limiting the Ioffe-Regel parameter to $k_{\text{eff}} \ell_s \gtrsim 1$ in Fig. S9b. The minimal value of $k_{\text{eff}} \ell_s$ is almost identical

for $f = 2.5\%$, 5% , 9% and starts to increase for $f = 18\%$ due to dependent scattering. The dependent scattering also results in less variation of the normalized transport mean free path $k_{\text{eff}} \ell_t$ with λ in Fig. S9c, similar to the scattering mean free path in Fig. S9b.

Diffusive nature of wave propagation in $n = 10$ dielectric systems can be seen from scaling of the CW transmittance with slab thickness L . In Fig. S9d we plot transmittance multiplied by L in the $f = 2.5\%$, 5% , 9% , 18% slabs with three different values of $L/\lambda_0 = 1, 2, 4$. The largest slab thickness $L/\lambda_0 = 4$ corresponds to $L/\ell_t > 36 \gg 1$ for all f . The overlap between the curves with different L in the spectral range of the first Mie resonance is a direct manifestation of the diffusive scaling $T \propto 1/L$.

Furthermore, we numerically calculate dynamic transmittance under pulsed excitation, $T(t)$. For thick slabs ($L/\ell_t \gg 1$), the system does not exhibit deviations from the diffusive transport: at $t \gg \tau_D$, the decay is still exponential (Fig. S9e).

The above results confirm the light transport is diffusive in 3D dielectric random systems with $n = 10$ spheres.

3 Difference between PEC and dielectric scattering

Besides the irrelevance of longitudinal fields in PEC composites for energy transport, additional differences with respect to dielectric media facilitate Anderson localization in PEC:

1. Isolated PEC spheres have strong backscattering (47). This results in a highly anisotropic angular scattering pattern, making $\ell_t < \ell_s$ at low f , which is very different from the dielectric spheres.
2. Collective scattering resonances are created by two or more adjacent PEC spheres. The spatial arrangement of scatterers in this work lacks spatial correlations in sphere positions, creating a random distribution of distance between them. Even at the PEC volume fraction

of $f = 8\%$, the gap in-between two PEC spheres can be much narrower than $\lambda = 650$ nm and the field intensity in the vicinity of the gap is strongly enhanced, as seen in Figs. S10a. Such an enhancement persists at $\lambda = 1080$ nm in Figs. S10b despite the wavelength being much greater than the particle radius $r = 50$ nm, leading to a small size parameter $kr \simeq 0.3 < 1$. Already for a volume fraction of $f = 8\%$, a sufficiently broad distribution of gap sizes creates a large number of red-shifted resonances, enhancing the overall scattering at longer wavelengths in Fig. 3a and making ℓ_s well below the prediction (S14) of the independent scattering approximation (ISA) $\ell_s = [\rho_{sca}(f) \sigma_{sca}(\lambda)]^{-1}$, where $\rho_{sca}(f)$ is the number density of scatterers and $\sigma_{sca}(\lambda)$ is the scattering cross-section of a single PEC sphere. With an increase of f to 15% in Figs. S10c,d, additional voids formed by three or more PEC spheres create even a larger variety of scattering resonances at different wavelengths, rendering ℓ_s nearly constant with λ .

3. At high volume fraction f of PEC scatterers, light propagation through air voids is suppressed. In contrast to a dielectric composite, which becomes transparent when the dielectric volume fraction approaches 100%, a PEC composite with f approaching 100% becomes a perfect mirror as air voids no longer percolate through the system. In our simulations, Anderson localization takes place at PEC volume fractions well below the air percolation threshold (96.6%) (S15, S11). Consider the Anderson model of random resonators (large air voids) connected by waveguides (narrow air channels). If the wavelength is larger than the waveguide diameter but smaller than the resonator size, the waveguides are below cut-off and transmission becomes evanescent, but light can still be confined in the resonators. The confined light may be coupled evanescently, hopping from one resonator to the next. The interference between waves following different paths from one void to another is essential to reach Anderson localization even when the transmission through the channels between voids is evanescent. In the absence of interference,

transport through a network of voids would be slowed down but still diffusive, no matter how weak the channel transmissions are. Eventually, in the infrared limit where the wavelength well exceeds the void size, light can no longer be confined in the voids, and the optical transport through the system will be blocked.

For a given PEC volume fraction f , both air void and air channel sizes are proportional to PEC sphere radius r . A random system with smaller spheres have a larger number of voids and channels, but the the latter have smaller sizes, since their total volume is fixed by f . Narrower channels make it harder for light to propagate through a system with smaller spheres, and localization will take place at lower f . This prediction agrees with our numerical results of lower critical f for AL with $r = 50$ nm PEC spheres than $r = 100$ nm spheres. The above argument is for fixed wavelength λ . In a PEC system with given values of r and f , the typical channel width a is fixed and therefore increasing λ will make it more difficult for light to ‘squeeze’ through the channels, facilitating AL at long wavelengths. Consequently, for a given r , the localization condition of $a \sim \lambda$ is fulfilled at a smaller f at longer λ , which is in agreement with our numerical results.

4 Additional evidence for Anderson localization in PEC system

4.1 Spatial intensity distribution

We have examined the intensity distributions inside 3D slabs of PEC spheres with $r = 50$ nm. Figure S11 shows the spatial distribution of intensity over a two-dimensional cross-section (x - z plane at $y = 0$) in the localized PEC system at five wavelengths (corresponding to the peaks of transmission spectrum in Fig. 2e). In the logarithmic scale of the intensity map, we see local regions of high intensity, sometimes a cluster of hot spots, even close-by bright regions that resemble necklace states. However, it is hard to tell whether they represent individual modes,

as the localized modes that are spatially separate may have nearly identical wavelength.

In the localization regime, there are many localized modes with similarly long lifetimes. Separating them would be difficult and require extremely long simulation time. Therefore, to find and visualize a single localized mode, we lower the PEC filling fraction to $f = 33\%$ to be close to the localization transition, where there are fewer localized modes with long lifetimes. After a long simulation time, the intensity decay approaches a single exponential decay of rate equal to the decay rate of the longest-lived mode. Figure S12 is a volumetric plot of this mode from two viewing angles. We also create a movie with rotating viewing angle (around y -axis), available as supporting material for this article.

Back to the localized system with PEC filling fraction of $f = 48\%$, we show in Fig. S13 the cross-section averaged depth profile at very long delay time, $\langle I(x, y, z; t \rightarrow \infty) \rangle_{x,y}$. For comparison, we also plot the asymptotic depth profile in the diffusive system of $f = 15\%$, which matches the first eigenmode of the diffusion equation, $\sin[\pi(z + z_0)/(L + 2z_0)]$. In contrast, the cross-section averaged intensity inside the localized slab with $f = 48\%$ exhibits a much larger variation with depth z . The faster decay towards the surfaces signifies stronger confinement of energy near the center of the slab.

4.2 Intensity statistics

The fluctuation of intensity or transmission coefficients is a powerful criterion of localization (9). We create a video showing the internal intensity distribution on x - z plane for $y = 0$, as the wavelength λ is continuously scanned in the range of our simulation. It provides a sharp contrast between diffusive and localized PEC systems. In the former (PEC filling fraction $f = 15\%$), the intensity pattern is more or less uniform across the system and it varies slowly with wavelength. In the latter ($f = 48\%$), the intensity fluctuates strongly from point to point and changes rapidly with λ .

Fig. S14a depicts spectral fluctuation of the cross-section averaged intensity $I(z, \lambda) = \langle I(x, y, z; \lambda) \rangle_{x,y}$, within the wavelength range of 600–700 nm. The normalized variance $\text{var}_\lambda[I(z, \lambda)]/\langle I(z, \lambda) \rangle_\lambda^2$ corresponds to the magnitude of long-range correlation C_2 (S16). In the PEC slab of $f = 15\%$, $C_2 \ll 1$, typical of a diffusive system. When f increases to 48%, $C_2 \geq 1$, as expected for localized systems (S14, S17), (9).

Inside a diffusive system, the CW intensity decays linearly with the depth on average (46) and exhibits weak fluctuations from configuration to configuration. This is confirmed in Fig. S14b by comparing $\langle I(z, \lambda) \rangle_\lambda$ and $\exp[\langle \log[I(z, \lambda)] \rangle_\lambda]$, which indeed agree well in the PEC slab of $f = 15\%$. In contrast, in the PEC slab of $f = 48\%$, c.f. Fig. S14c, these two quantities are markedly different due to the fact that strong intensity fluctuations lead to log-normal distribution for localized systems (S18). The depth profile exhibits a roughly exponential decay, as expected in the AL regime of transport.

We confirm the statistical distribution of field intensity is log-normal in the Anderson localization regime by a statistical analysis. Fig. S15 shows the probability density function (PDF) of $\log(I_y/\langle I_y \rangle)$, where $I_y = |E_y(x, y, L)|^2$ is the intensity of the cross-polarized field (parallel to y -axis, while the incident field is x -polarized) close to the output surface of the localized PEC slab in Fig. 2e of the main text, and it is normalized by the average over λ , $\langle I_y \rangle$. $P[\log(I_y/\langle I_y \rangle)]$ fits well by a Gaussian function (red curve in Fig. S15), verifying the log-normal distribution. It is further contrasted from the logarithmic intensity PDF of the diffusive PEC system (blue symbols) in Fig. 2d. The latter satisfies the Rayleigh intensity statistics (blue curve), $P(I_y/\langle I_y \rangle) = (1/\langle I_y \rangle) \exp(-I_y/\langle I_y \rangle)$.

4.3 Thouless criterion

We quantify the Thouless conductance for the diffusive and localized PEC slabs in Fig. 2d,e of the main text. As shown in Fig. S16a, the intensity spectra at a single position $(0, 0, z)$ on

the output surface of the slab appear dramatically different for diffusive and localized systems. Quantitatively, we compute the spectral field correlation function, $C_E(\Delta\omega) = \langle E_y^*(x, 0, L; \omega + \Delta\omega) E_y(x, 0, L; \omega) \rangle_{x,\omega} / \langle |E_y(x, 0, L; \omega)|^2 \rangle_{x,\omega}$. Fig. S16b plots $|C_E(\Delta\omega)|^2$ versus frequency detuning $\Delta\omega$, which is normalized by the average mode spacing $\Delta\omega_{DOS}$. We calculate $\Delta\omega_{DOS} = [\omega^2 / (\pi^2 c^3) (1 - f) V]^{-1}$, where $\omega^2 / (\pi^2 c^3)$ is the density of states in vacuum, $(1 - f)$ is the vacuum filling fraction in the PEC slab, $V = L^3$ is the volume of a cube of side L equal to the slab thickness. The width of $|C_E(\Delta\omega / \Delta\omega_{DOS})|^2$ gives the ratio of the average mode linewidth over the average mode spacing, which is equal to the Thouless conductance. Its value is 7.1 for the diffusive PEC slab, and 0.28 for the localized one. These values agree with the Thouless criterion for localization.

4.4 Larger PEC spheres

To further confirm AL in PEC slabs, we repeat the calculations reported in Fig. 3c,d for another system with larger PEC spheres ($r = 100$ nm). Figure S17 shows that transmittance and conductance exhibit similar scaling behaviors as for the PEC slabs of $r = 50$ nm in Fig. 3c,d. Although the diffusion-localization transition occurs at a different volume filling fraction f of PEC spheres, the scaling behaviors with respect to the Ioffe-Regel parameter $k \ell_s$ and to the dimensionless conductance g are reproduced.

5 Anderson localization in real metals

The perfect electric conductor (PEC) is an ideal metal that has no absorption. Scattering cross-sections of PEC spheres with different radii are shown in Fig. S18a. To show the possibility of AL in realistic metallic systems, we simulate real metals using parameters reported in literature. The dielectric constant of a metal is related to the conductivity $\sigma(\omega)$ via $\epsilon(\omega) = 1 + i\sigma(\omega)/\omega\epsilon_0$, where ϵ_0 is electric permittivity of vacuum. In the Drude model, the conductivity of a metal is

given by $\sigma(\omega) = \sigma_0/(1 - i\omega\tau)$, where σ_0 is the static conductivity and τ is the relaxation time.

5.1 Microwave regime

At microwave frequencies, $\omega \ll 1/\tau$ and $\epsilon(\omega) \simeq 4\pi\sigma_0 i/\omega$. The penetration depth of electric field into the metal is characterized by the skin depth $\sim (\lambda_0/2\pi) (\omega/2\pi\sigma_0)^{1/2}$. Common metals like silver, aluminum, and copper have low loss and large conductivity at microwave frequencies, and their skin depth is much shorter than the wavelength. For example, at 20 GHz where the wavelength is 1.5 cm, the skin depth is less than 1 μm (S19).

To simulate microwave transport in 3D aggregates of metallic spheres, we generate random arrangements of overlapping spheres with the same procedure as used for the PEC systems. The sphere diameter of 0.56 cm is four orders of magnitude larger than the skin depth of crystalline metals like silver, aluminum, copper. Thus, the microwave barely penetrates into the metallic scatterers and the absorption loss is negligible. When we use the conductivity $\sigma_0 = 3.8 \times 10^7 \Omega^{-1}/\text{m}$ of crystalline aluminum reported in literature (S19), the scattering cross-section of an aluminum sphere barely deviates from that for PEC (Fig. S18b).

However, experimentally fabricated metallic structures have additional losses due to polycrystallinity, surface defects, oxide layers, etc. To take these into account, we lower the conductivity σ_0 so that the simulated transport properties match the experimental values in Ref. (29). Specifically, we simulate dynamic transmittance in a diffusive slab of aluminum spheres with the same volume fraction $f = 35\%$ and slab thickness $L = 6$ cm as in the experiment. When the conductivity is reduced to $\sigma_0 = 3.8 \times 10^4 \Omega^{-1}/\text{m}$, our simulated diffusion coefficient $D = 1.9 \times 10^9 \text{ cm}^2/\text{s}$ and absorption coefficient $\alpha = (D\tau_a)^{-1} \simeq 0.2 \text{ cm}^{-1}$ both agree to the experimental values at 20 GHz. Using these realistic parameters, we simulate 3D metallic composites with high volume fractions of $f = 60\%$. As shown in Fig. S19a, the apparent diffusion coefficient, obtained from the temporal decay of the transmittance without taking absorption

into account, decreases in time as $1/t$, similarly to its behavior in PEC, until it reaches the value set by the absorption. The simulated field intensity distribution inside the system, in Fig. S19b, provides evidence of spatial confinement of microwave, similar to the result for PEC in Fig. 2e. The most conclusive evidence of AL is the arrest of transverse spreading of transmitted wave field. It is insensitive to absorption as shown in the main text in Fig. 4e.

We believe that the tell-tale experimental sign of AL is the arrest of transverse spreading of transmitted wave with a focused incident pulse. Potential pitfalls include background signals or possible emission by the metal upon microwave excitation. However, these signals are typically broadband and incoherent with the incident wave. If the incident microwave has a narrow spectral band, the transmitted field may be measured coherently, e.g., using the homodyne technique common for microwaves, when those background and incoherent signals will not contribute. Hence, we propose an experiment with a frequency-tunable narrowband microwave source: focus the incident microwave to the front surface of a slab and scan the frequency, perform an interferometric measurement of transmitted field distribution near the slab back surface at each frequency (using a local oscillator), finally Fourier transform the spectral fields to reconstruct the temporal evolution of transmitted field for an incident short pulse in order to detect the arrest of transverse spreading.

5.2 Optical regime

Here we investigate the possibility of AL of visible light in 3D metallic nanostructures. Even for low-loss metals like gold and silver, the skin depth is ~ 25 nm at $\lambda = 650$ nm (S19), comparable to the nanoparticle diameter of 100–200 nm. A significant penetration of light field inside the metal particles makes them deviate from the PEC, which expels the fields completely. Another consequence of the penetration is a notable loss. We simulate silver, which is widely used in nano-plasmonics and meta-materials, using realistic parameters reported in the literature. We

adopt the Drude model of $\epsilon(\omega)$ with $\sigma_0 \simeq 6.1 \times 10^7 \text{ } \Omega^{-1}/\text{m}$ and $\tau \simeq 3.7 \times 10^{-14} \text{ s}$ from Ref. (S20). Despite absorption and deviation from PEC, we still detect the arrest of transverse spreading in Fig. S20.

Compared to 2D nanostructures, 3D nanoporous metals have a much larger (internal) surface area, leading to a wide range of applications in photo-catalysis (S21), optical sensing (S22), energy conversion and storage (S23). Metallic nanostructures have been widely explored to enhance Raman scattering, second-harmonic generation, etc., because they can produce ‘hot spots’ (giant local fields) to boost optical nonlinearities. Also metallic nanoparticles have been used for random lasing, as their strong scattering of light improves optical feedback (S24, S25). Our simulation results suggest the possibility of AL in 3D metallic nanostructures at optical frequencies. Light localization in such structures will have a significant impact on optical nonlinear, lasing, photochemical processes and related applications.

Supplementary References

- [S1] Osnabrugge, G., Leedumrongwathanakun, S. & Vellekoop, I. M. A convergent born series for solving the inhomogeneous helmholtz equation in arbitrarily large media. *Journal of computational physics* **322**, 113–124 (2016).
- [S2] Krüger, B., Brenner, T. & Kienle, A. Solution of the inhomogeneous maxwell’s equations using a born series. *Optics express* **25**, 25165–25182 (2017).
- [S3] Xu, Y. L. & Gustafson, B. A generalized multiparticle Mie-solution: further experimental verification. *J. Quant. Spectr. Rad. Transf.* **70**, 395–419 (2001). Light Scattering by Non-Spherical Particles.
- [S4] Pellegrini, G., Mattei, G., Bello, V. & Mazzoldi, P. Interacting metal nanoparticles: Optical properties from nanoparticle dimers to core-satellite systems. *Mat. Sci. Eng. C* **27**, 1347–1350 (2007).
- [S5] Egel, A. *et al.* Smuthi: A python package for the simulation of light scattering by multiple particles near or between planar interfaces. *J. Quant. Spectr. Rad. Transf.* **273**, 107846 (2021).
- [S6] Mackowski, D. & Mishchenko, M. A multiple sphere t-matrix fortran code for use on parallel computer clusters. *J. Quant. Spectr. Rad. Transf.* **112**, 2182–2192 (2011).
- [S7] Gumerov, N. A. & Duraiswami, R. Computation of scattering from clusters of spheres using the fast multipole method. *The Journal of the Acoustical Society of America* **117**, 1744–1761 (2005).

- [S8] Egel, A., Pattelli, L., Mazzamuto, G., Wiersma, D. S. & Lemmer, U. Celes: Cuda-accelerated simulation of electromagnetic scattering by large ensembles of spheres. *J. Quantitative Spectroscopy and Radiative Transfer* **199**, 103–110 (2017).
- [S9] Conti, C. & Fratolocci, A. Dynamic light diffusion, three-dimensional Anderson localization and lasing in inverted opals. *Nat. Phys.* **4**, 794–798 (2008).
- [S10] Taflove, A., Hagness, S. C. & Picket-May, M. *Computational electromagnetics: the finite-difference time-domain method*, 629–670 (Elsevier, 2005).
- [S11] Elam, W. T., Kerstein, A. R. & Rehr, J. J. Critical properties of the void percolation problem for spheres. *Phys. Rev. Lett.* **52**, 1516–1519 (1984).
- [S12] Torquato, S. Hyperuniform states of matter. *Phys. Rep.* **745**, 1–95 (2018). Hyperuniform States of Matter.
- [S13] Lagendijk, A. & van Tiggelen, B. A. Resonant multiple scattering of light. *Phys. Rep.* **270**, 143–215 (1996).
- [S14] van Rossum, M. C. & Nieuwenhuizen, T. M. Multiple scattering of classical waves: microscopy, mesoscopy, and diffusion. *Rev. Mod. Phys.* **71**, 313–371 (1999).
- [S15] Kertész, J. Percolation of holes between overlapping spheres : Monte carlo calculation of the critical volume fraction. *J. Physique Lett.* **42**, 393–395 (1981).
- [S16] Sarma, R., Yamilov, A., Neupane, P., Shapiro, B. & Cao, H. Probing long-range intensity correlations inside disordered photonic nanostructures. *Phys. Rev. B* **90**, 014203 (2014).
- [S17] Chang, S. H., Taflove, A., Yamilov, A., Burin, A. & Cao, H. Numerical study of light correlations in a random medium close to the Anderson localization threshold. *Opt. Lett.* **29**, 917–919 (2004).

- [S18] Mirlin, A. Statistics of energy levels and eigen-functions in disordered systems. *Phys. Rep.* **326**, 259–382 (2000).
- [S19] Li, Y. (ed.) *Plasmonic Optics: Theory and Applications* (SPIE press, 2017).
- [S20] Ordal, M. A., Bell, R. J., Alexander, R. W., Long, L. L. & Querry, M. R. Optical properties of fourteen metals in the infrared and far infrared: Al, co, cu, au, fe, pb, mo, ni, pd, pt, ag, ti, v, and w. *Appl. Opt.* **24**, 4493–4499 (1985).
- [S21] Linic, S., Christopher, P. & Ingram, D. B. Plasmonic-metal nanostructures for efficient conversion of solar to chemical energy. *Nature materials* **10**, 911–921 (2011).
- [S22] Chen, L.-Y., Yu, J.-S., Fujita, T. & Chen, M.-W. Nanoporous copper with tunable nanoporosity for sers applications. *Advanced Functional Materials* **19**, 1221–1226 (2009).
- [S23] Mascaretti, L. *et al.* Plasmon-enhanced photoelectrochemical water splitting for efficient renewable energy storage. *Advanced Materials* **31**, 1805513 (2019).
- [S24] Wang, Z., Meng, X., Kildishev, A. V., Boltasseva, A. & Shalaev, V. M. Nanolasers enabled by metallic nanoparticles: from spasers to random lasers. *Laser & Photonics Reviews* **11**, 1700212 (2017).
- [S25] Gomes, A. S., Moura, A. L., de Araújo, C. B. & Raposo, E. P. Recent advances and applications of random lasers and random fiber lasers. *Progress in Quantum Electronics* **78**, 100343 (2021).

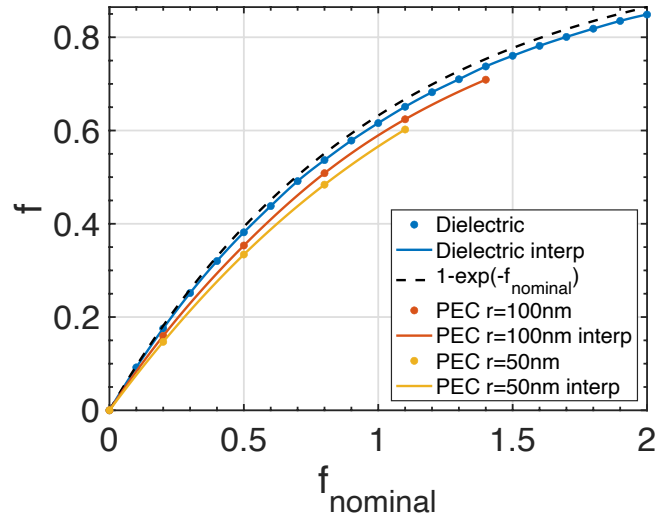


Figure S1: **Dielectric/PEC filling fraction of simulated aggregates of randomly positioned spheres.** Mapping between the actual volume filling fraction f (accounting for sphere overlap and discretization effects) and the nominal filling fraction f_{nominal} .

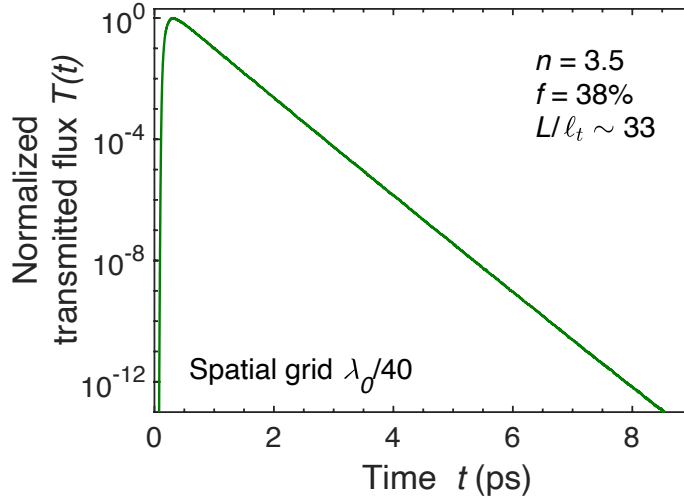


Figure S2: **Confirmation of the absence of Anderson localization in random dielectric media with refractive-index of 3.5 with increased numerical resolution.** Transmittance $T(t)$ of an optical pulse through a 3D slab of thickness $L = 3.3 \mu\text{m}$, filled with dielectric spheres at random uncorrelated positions (radius $r = 100 \text{ nm}$, refractive index $n = 3.5$, volume filling fraction $f = 38\%$) in air. Numerical simulations are performed with a spatio-temporal discretization of $\lambda_0/40$, which is twice finer than that used to produce Fig. 1e in the main text. The pure exponential decay of $T(t)$ in time, over 12 orders of magnitude, is a hallmark of diffusive transport in the dielectric random system.

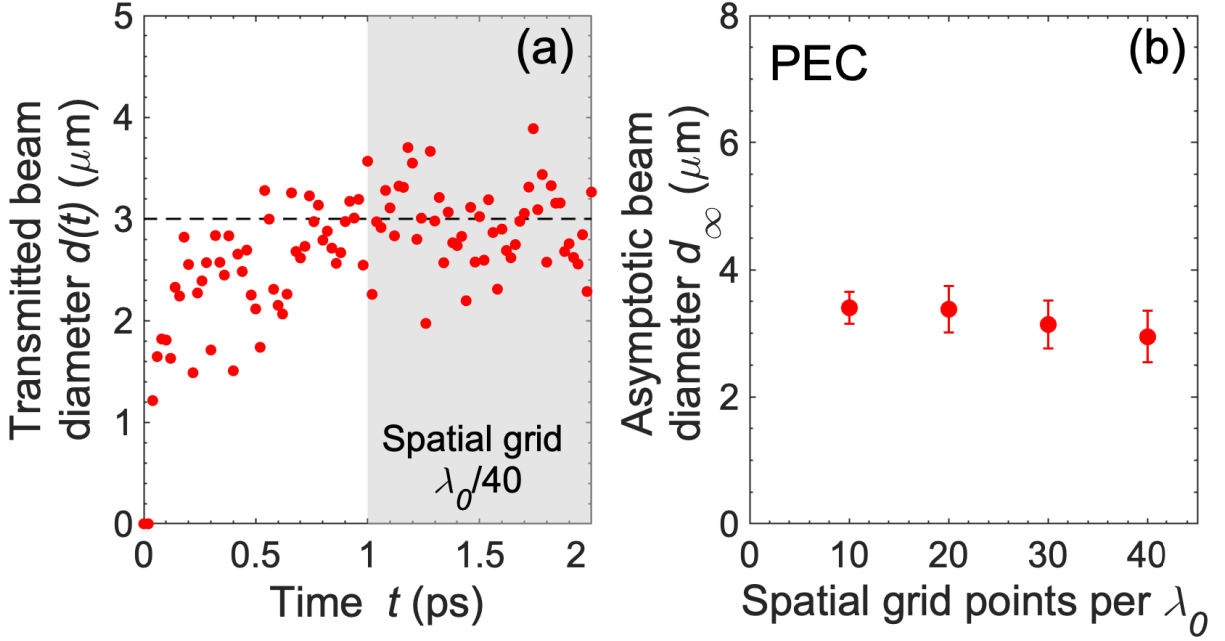


Figure S3: **Robustness of the arrest of transverse spreading of transmitted beam in localized PEC systems against numerical discretization.** The simulation is schematically depicted in Fig. 4a of the main text, and the structure parameters (sphere radius $r = 50$ nm, volume filling fraction $f = 48\%$) are identical to those in Fig. 4d. a, Transverse diameter of the transmitted beam $d(t)$, obtained from numerical simulation (slab thickness $L = 1.3 \mu\text{m}$) with $\lambda_0/40$ resolution, exhibits a saturation consistent with the result with $\lambda_0/20$ resolution in Fig. 4d. b, Arrest of the transverse spreading is seen in all simulations performed with numerical resolution from $\lambda_0/10$ to $\lambda_0/40$ with a consistent asymptotic transverse beam diameter d_∞ . Symbols and error-bars represent the mean value and standard deviation of $d(t)$ in the time interval $1 \text{ ps} < t < 2 \text{ ps}$ (gray area in panel a, i.e. over sample size of 50 data points).

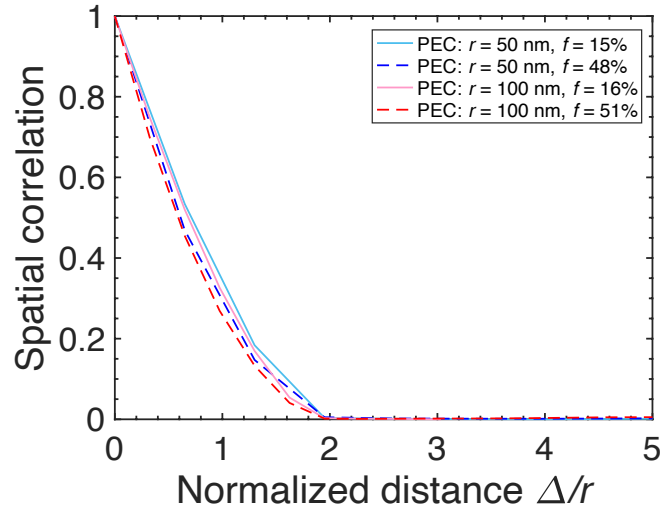


Figure S4: **Spatial correlation in PEC composites.** Normalized spatial correlation function $C(\Delta)/C(0)$ for random aggregates of overlapping spheres with radii $r = 50$ nm, 100 nm and volume filling fractions $f \simeq 15\%, 50\%$. Spatial correlation vanishes beyond one sphere diameter $2r$.

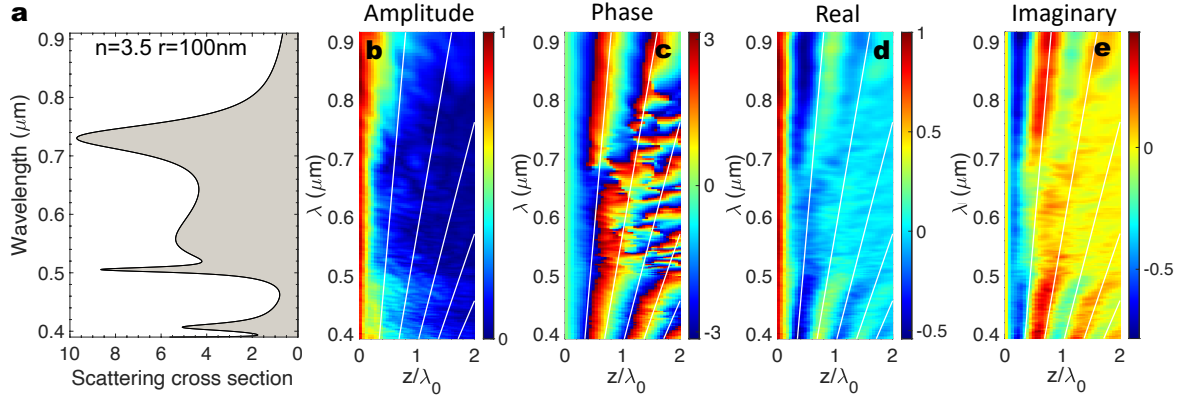


Figure S5: **Extinction of coherent field in a dielectric slab of $n = 3.5$ spheres.** a, Scattering cross-section of a single dielectric sphere of radius $r = 100$ nm and refractive index $n = 3.5$ in air, normalized by the geometrical cross-section. The spectral peaks correspond to Mie resonances. b,c,d,e, amplitude (b), phase (c), real (d) and imaginary (e) parts of coherent field $\langle E_x(x, y_0, z; \lambda) \rangle_x$ versus depth z and wavelength λ for dielectric filling fraction $f = 29\%$. White lines represent $z = m\lambda_{\text{eff}}$, where m is an integer and $\lambda_{\text{eff}} = \lambda/n_{\text{eff}}$. The coherent field amplitude experiences an enhanced extinction in the wavelength range 500–700 nm due to hybridized Mie resonances.

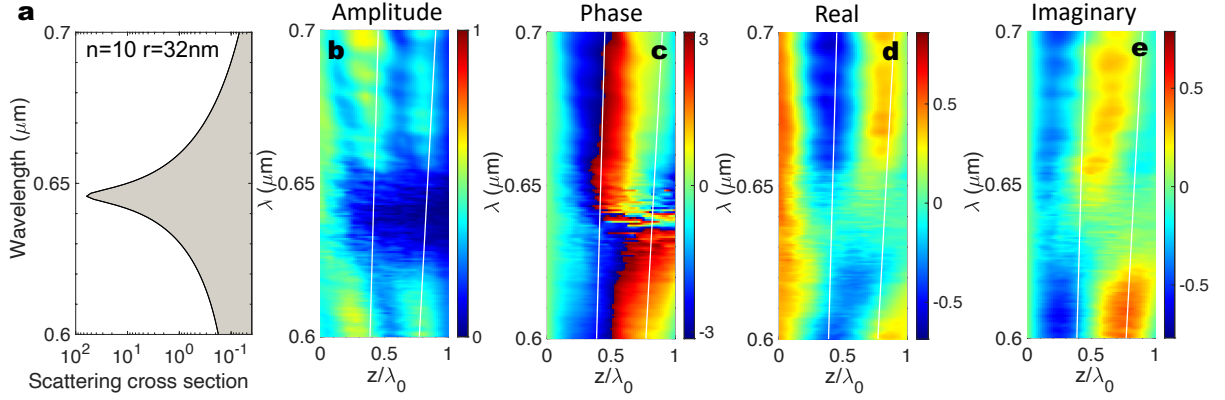


Figure S6: **Extinction of coherent field in a dielectric slab of $n = 10$ spheres.** a, Scattering cross-section of a single dielectric sphere of radius $r = 32$ nm and refractive index $n = 10$ in air, normalized by the geometrical cross-section. The peak represents the first Mie resonance of magnetic dipole origin. b,c,d,e, amplitude (b), phase (c), real (d) and imaginary (e) parts of coherent field $\langle E_x(x, y_0, z; \lambda) \rangle_x$ versus depth z and wavelength λ for dielectric filling fraction $f = 29\%$. White lines represent $z = m\lambda_{\text{eff}}$, where m is an integer and $\lambda_{\text{eff}} = \lambda/n_{\text{eff}}$. The coherent field amplitude experiences an enhanced extinction in the spectral range 630–660 nm in the vicinity of the first Mie resonance.

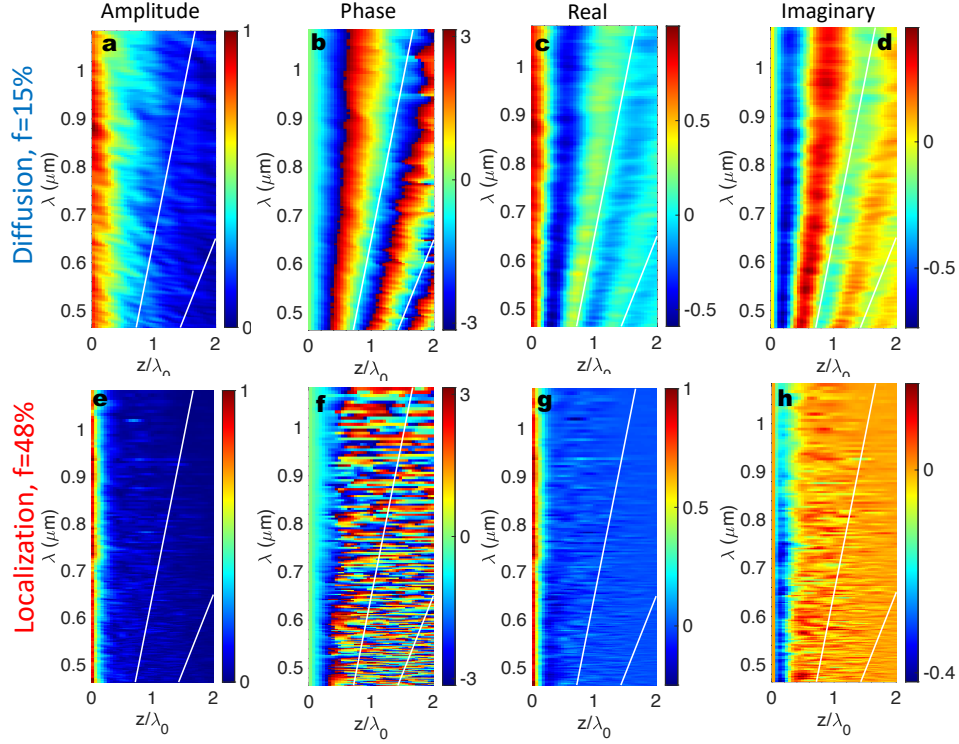


Figure S7: **Comparison of coherent fields in diffusive and localized slabs of PEC spheres.** Amplitude (a,e), phase (b,f), real (c,g) and imaginary (d,h) parts of coherent field $\langle E_x(x, y_0, z; \lambda) \rangle_x$ versus depth z and wavelength λ for PEC filling fraction $f = 15\%$ (a,b,c,d) and 48% (e,f,g,h). White lines represent $z = m\lambda$, where m is an integer. In the localized slab ($f = 48\%$), the extinction of the coherent field is much stronger and nearly independent of wavelength.

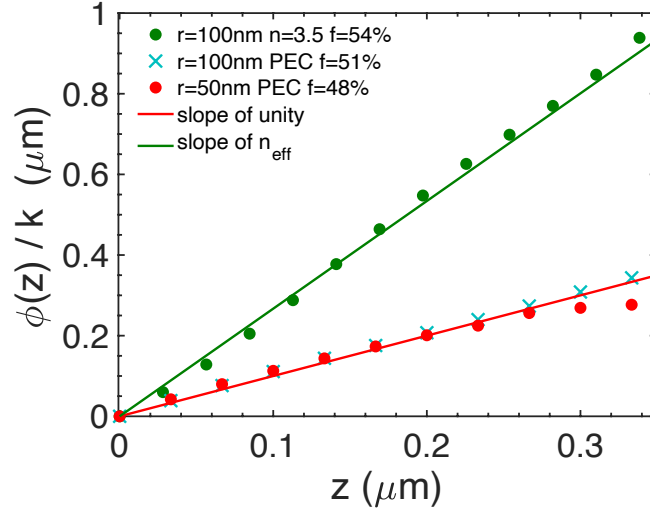


Figure S8: **Estimation of effective wavenumber k_{eff} .** The phase $\phi(z)$ of the average co-polarized coherent field, normalized by vacuum wavenumber k , grows linearly with depth z near the front surface of both dielectric (green circle) and PEC (red circle: $r = 50$ nm, cyan cross: $r = 100$ nm) slabs. Green and red lines are linear fits, which gives slopes of n_{eff} and unity, respectively.

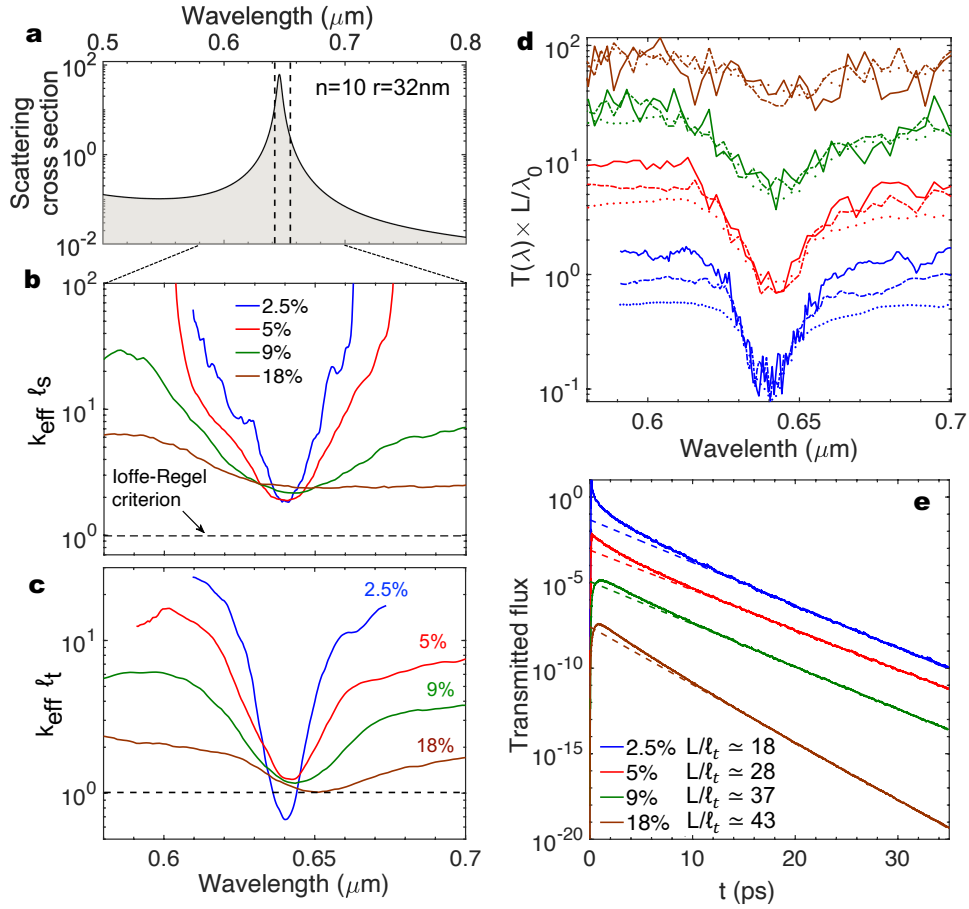


Figure S9: **Resonant scattering and diffusion in random ensembles of $n = 10$ dielectric spheres.** a, Scattering cross-section of a single dielectric sphere of radius $r = 32$ nm and refractive index $n = 10$, normalized by the geometrical cross-section. The vertical dotted lines mark the spectral width of the excitation pulse in panel e. b, Resonantly enhanced scattering mean free path ℓ_s in the spectral vicinity of the first Mie resonance of single-particle scattering. The dielectric filling fraction $f = 2.5\%$ (blue), $f = 5\%$ (red), 9% (green) and 18% (brown). The minimum Ioffe-Regel parameter $k_{\text{eff}} \ell_s \sim 2$. The horizontal dashed line marks the Ioffe-Regel criterion $k_{\text{eff}} \ell_s = 1$ for 3D localization. c, Normalized transport mean free path $k_{\text{eff}} \ell_t$ in the spectral vicinity of the first Mie resonance, reflecting saturation by dependent scattering between $f = 2.5\%$ and 18% . d, CW transmittance $T(\lambda)$ for three slab thicknesses $L/\lambda_0 = 1, 2, 4$ (solid, dashed, and dotted lines). $T(\lambda)$ multiplied by L/λ_0 remains nearly independent of L at wavelengths around minimum transmission, reflecting the diffusive scaling of $T \propto 1/L$. Results are color-coded as in panels b,c. For $f = 5\%$, 9% and 18% , the curves are shifted up vertically by one, two, and three decades for legibility. e, Transmittance of 3D slabs with thickness $L = 2 \lambda_0$ for pulsed excitation, showing an exponential decay (dashed lines) in time at long delay. The decay rate is determined by the minimum diffusion coefficient within the pulse bandwidth. Legend shows values of L/ℓ_t in each system. For $f = 5\%$, 9% and 18% , the curves are shifted down vertically by two, four and six decades for legibility.

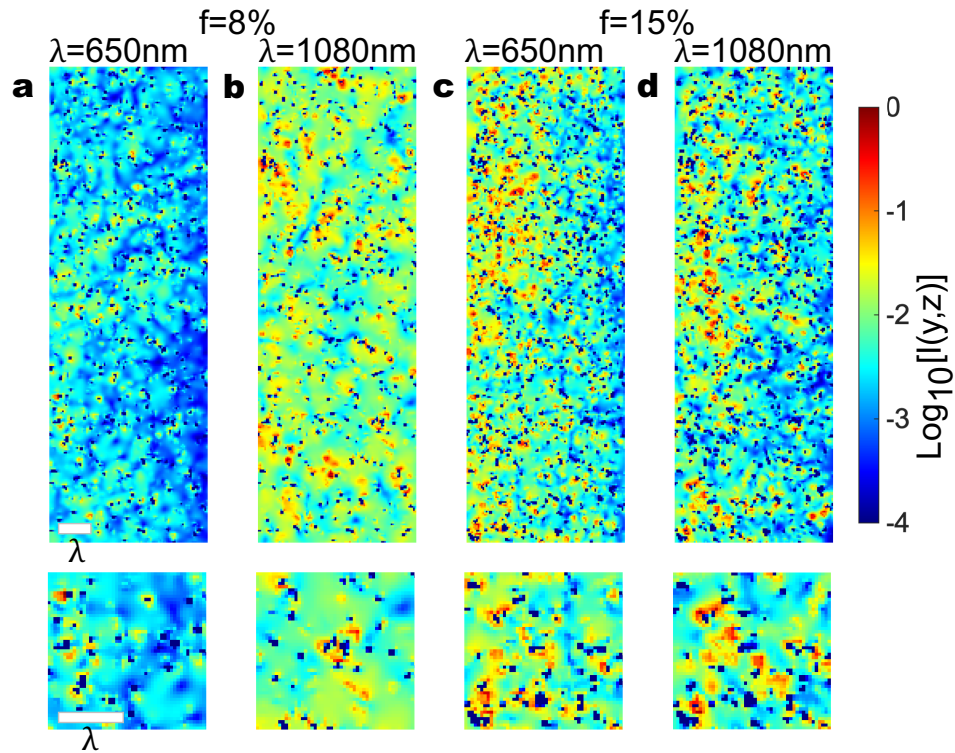


Figure S10: **Spatial intensity distribution inside disordered PEC system.** Field intensity at a (y, z) cross-section inside a random ensemble of PEC spheres with radius $r = 50$ nm. PEC filling fraction is $f = 8\%$ in panels a,b and $f = 15\%$ in panels c,d. $\lambda = 650$ nm in panels a,c and 1080 nm in panels b,d. The bottom row shows a magnified view of each distribution in the top row, revealing strong intensity enhancement in air voids between PEC particles due to coupled resonances. The size of the voids can be much smaller than the wavelength λ indicated by the white scale bar.

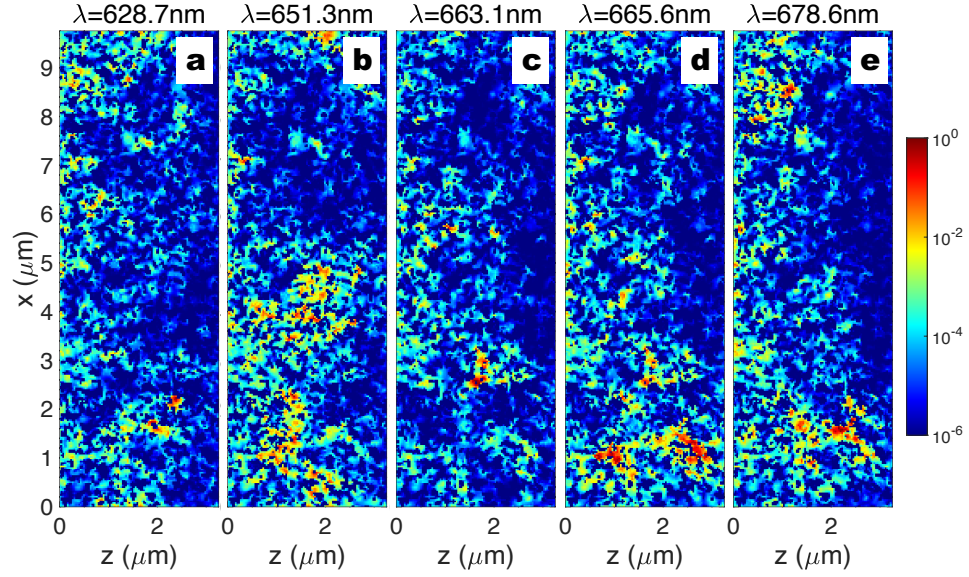


Figure S11: **Intensity distribution inside localized system.** Field intensity $I(x, 0, z; \lambda)$ distribution over the $y = 0$ cross section ($x - z$ plane) in the localized PEC slab (Fig. 2e) at five wavelengths. The wavelengths are selected to correspond to peaks of the transmission spectrum in Fig. 2e.

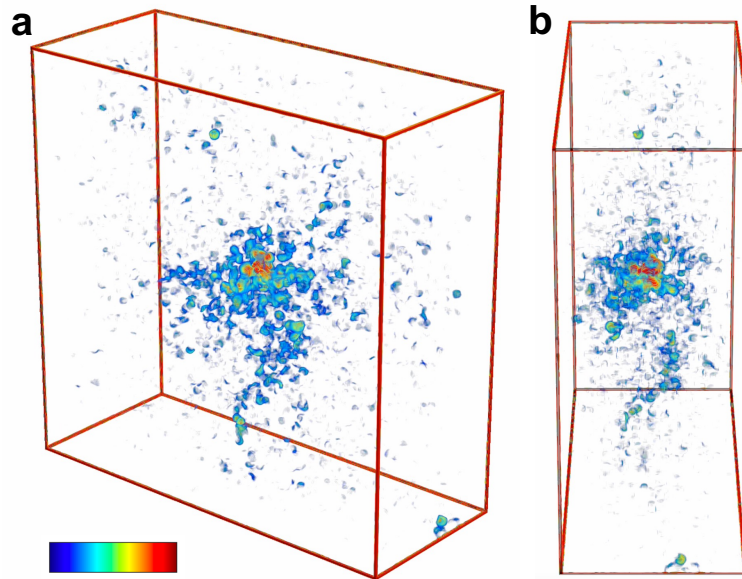


Figure S12: **3D localized mode in disordered PEC system.** Volumetric plot of a localized mode in a slab with $f = 33\%$ made up of overlapping PEC spheres with radius $r = 50$ nm. Panels a,b show the same state from two different viewing angles.

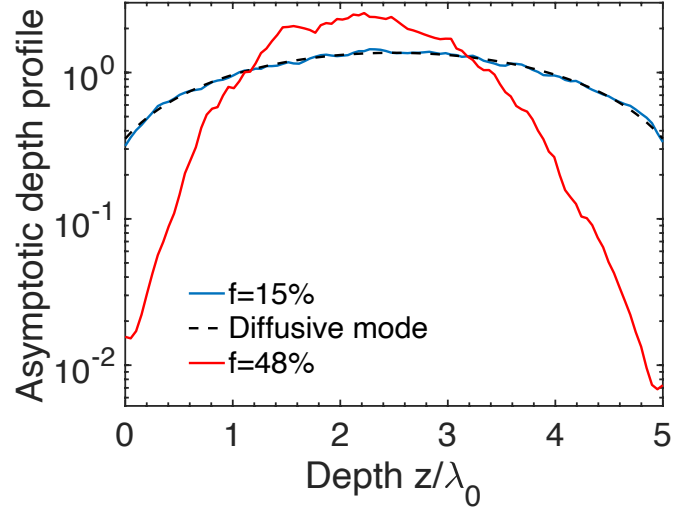


Figure S13: **Asymptotic depth profiles of intensity in disordered PEC.** a, Depth profile $\langle I(x, y, z; t \rightarrow \infty) \rangle_{x, y}$ inside the PEC slab of $f = 15\%$ (blue solid line) and 48% (red solid line). The lowest-order diffusive mode profile (black dashed line) matches that of $f = 15\%$ (blue).

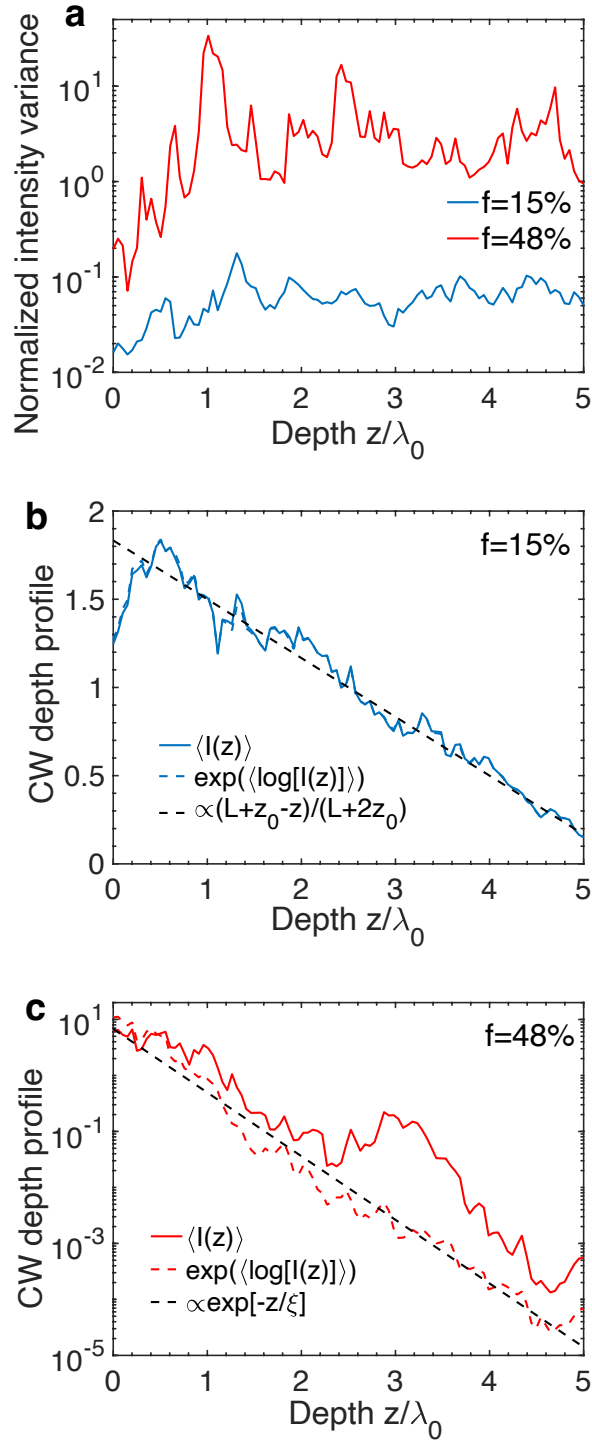


Figure S14: **Intensity statistics in disordered PEC.** a, Normalized variance of cross-section integrated intensity, showing two orders of magnitude enhancement of intensity fluctuations for $f = 48\%$ over $f = 15\%$. b,c, CW intensity depth profiles $\langle I(z, \lambda) \rangle_\lambda$ (solid lines) and $\exp[\langle \log[I(z, \lambda)] \rangle_\lambda]$ (dashed lines), compared to linear decay for $f = 15\%$ and exponential decay for $f = 48\%$ (black dashed lines).

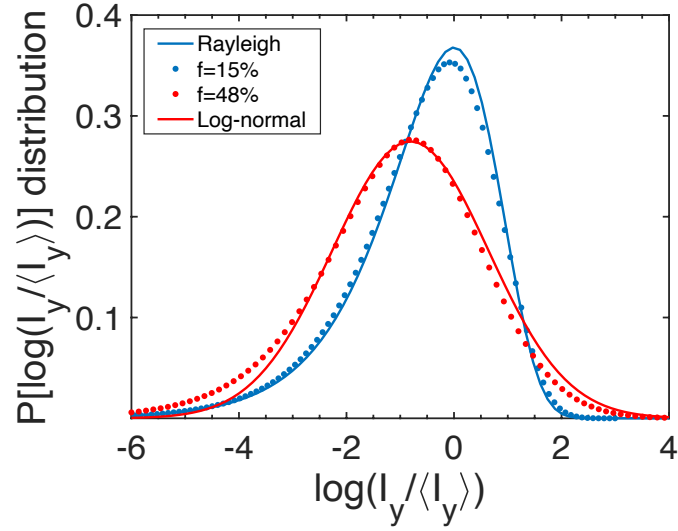


Figure S15: **Statistical distribution of transmitted intensity in disordered PEC.** Probability density of the logarithm of transmitted field intensity $I_y = |E_y(x, y, L)|^2$ (normalized by its mean $\langle I_y \rangle$) from Fig. 2e (red symbols) in the localized system is fit well by a Gaussian function (red curve). It is distinct from that in the diffusive system from Fig. 2d (blue symbols), which is fit well by the Rayleigh intensity statistics (blue curve).

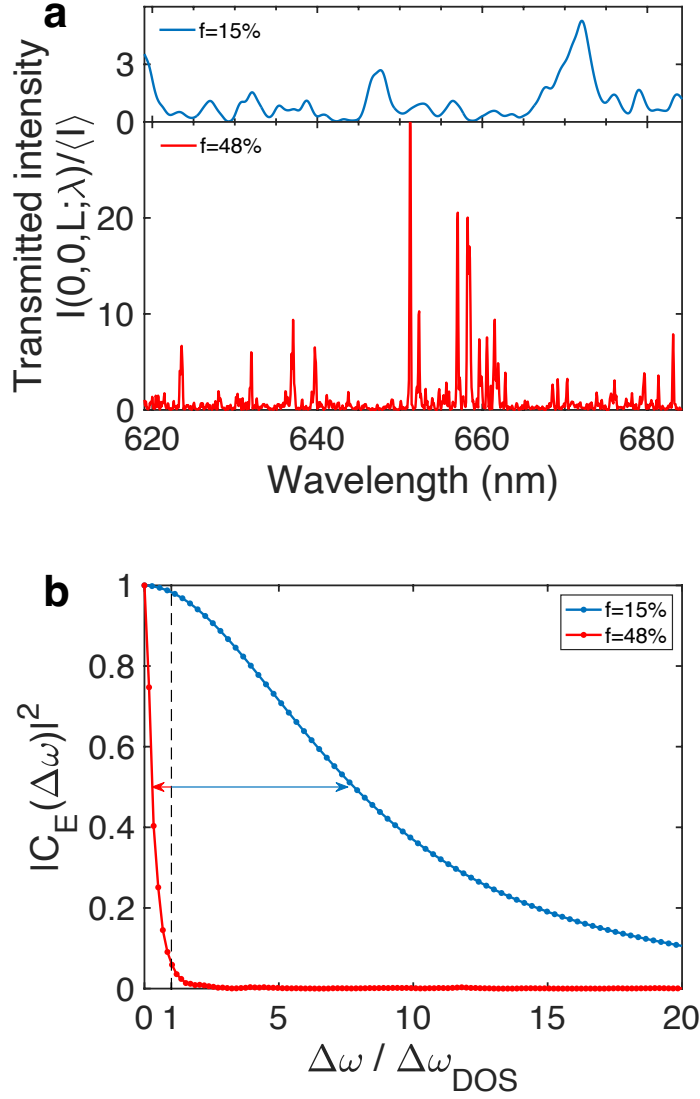


Figure S16: **Thouless criterion in disordered PEC.** a, Normalized intensity at location $(0, 0, L)$ of the output surface of the diffusive slab of PEC filling fraction $f = 15\%$ (blue line), and of the localized slab with $f = 48\%$ (red line). b, Spectral field correlation function squared $|C_E|^2$ vs. frequency detuning $\Delta\omega$ normalized by the average mode spacing $\Delta\omega_{DOS}$.

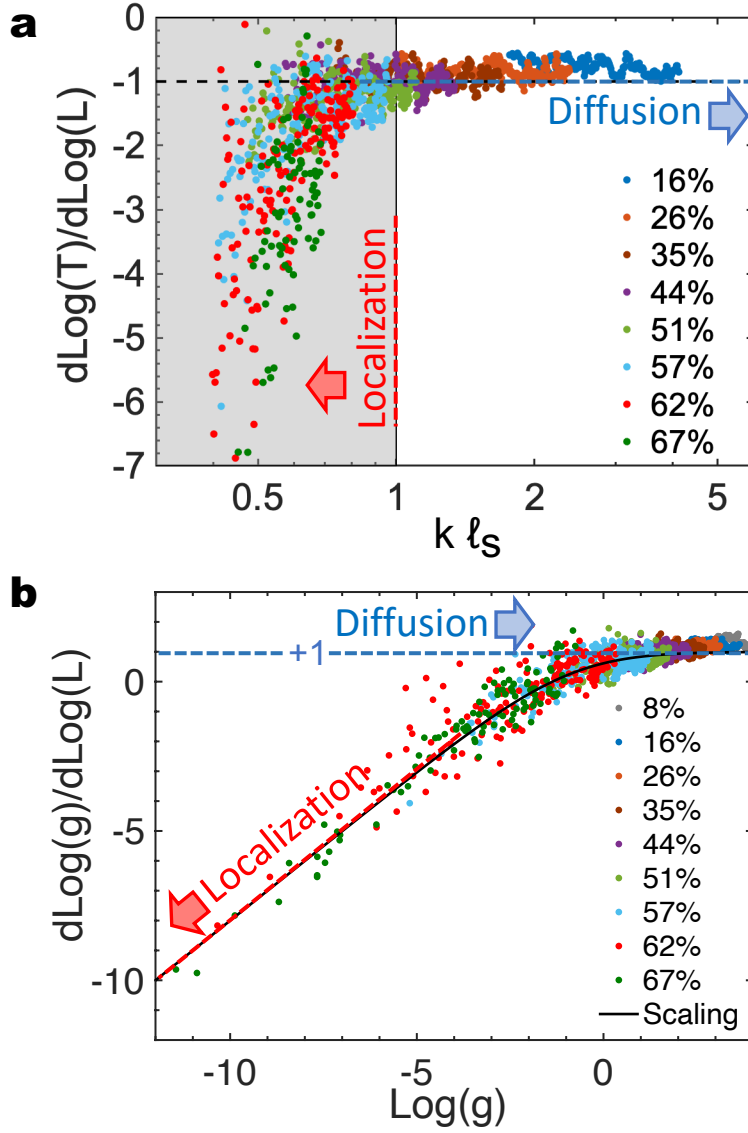


Figure S17: **Diffusion-localization transition in another PEC system with larger spheres.** The scaling behavior reported in Fig. 3b,c is reproduced for a system of larger PEC spheres with radius $r = 100$ nm, even though the diffusion-localization transition occurs at a different volume filling fraction f of PEC spheres. In a, the blue dashed line denotes diffusive scaling $T \propto L^{-1}$; the red dashed line marks $k\ell_s = 1$. In b, the blue and red dashed lines denote diffusive and localized scaling $g \propto L$ and $g \propto \exp(-L/\xi)$ respectively, where ξ is the localization length.

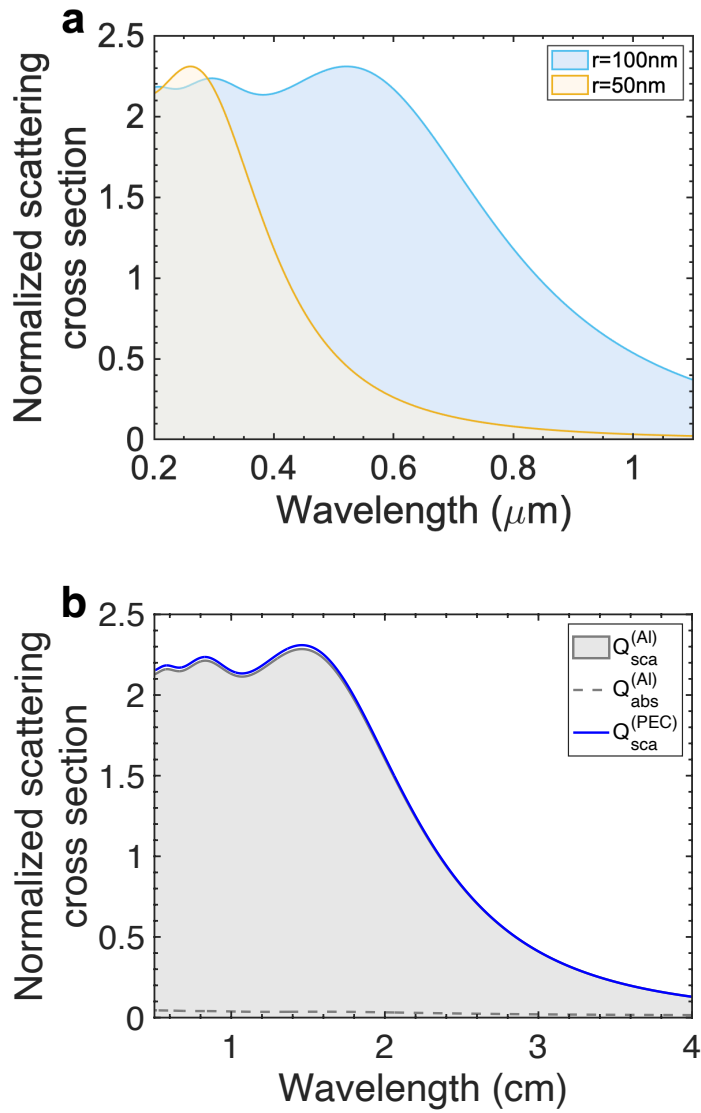


Figure S18: **Scattering cross-section of PEC and aluminum spheres.** (a) Scattering cross-section of a PEC sphere with radius $r = 50\ \text{nm}$ (yellow), $100\ \text{nm}$ (blue), normalized by the geometrical cross-section. (b) Scattering cross-section of an aluminum sphere with $r = 0.56\ \text{cm}$ and $\sigma_0 = 3.8 \times 10^4\ \Omega^{-1}/\text{m}$ in the microwave regime (gray), normalized by the geometrical cross-section. It is almost identical to that of a PEC sphere with the same radius (blue line).

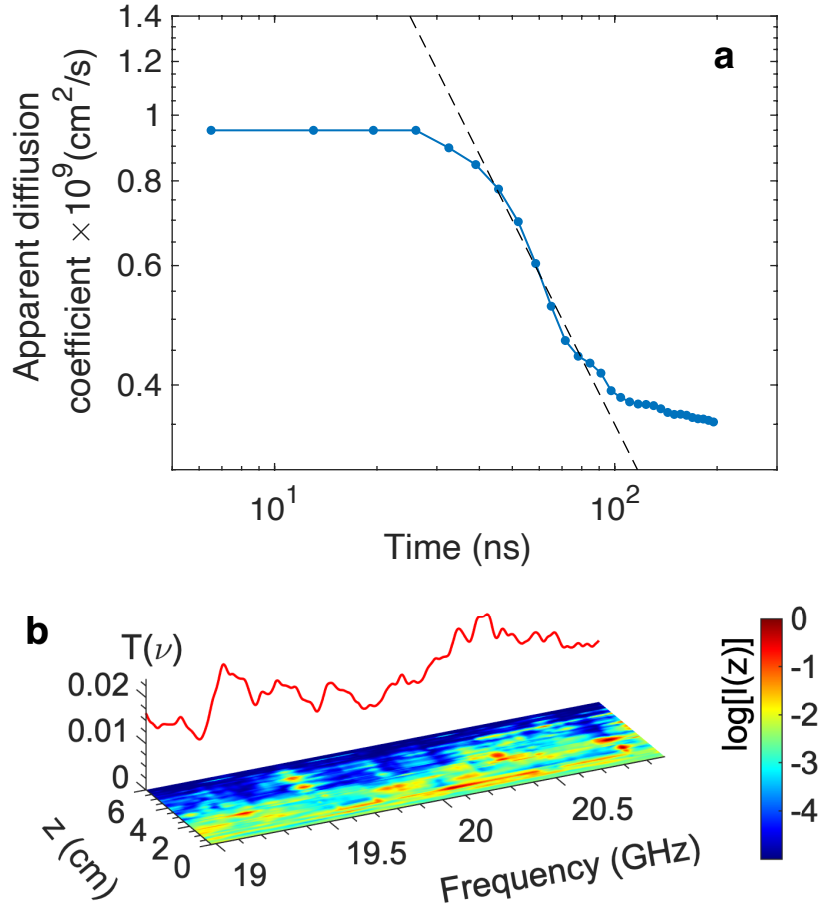


Figure S19: **Localization of microwaves in a 3D real-metal composite.** A random aggregate of aluminum spheres with radius $r = 0.28$ cm, realistic conductivity $\sigma_0 = 3.8 \times 10^4 \Omega^{-1}/\text{m}$, and volume filling fraction $f = 60\%$ localizes microwave of frequency around 20 GHz in a slab of thickness $L = 6$ cm. a, Time-resolved apparent diffusion coefficient $D(t)$, extracted from the temporal decay rate of $T(t)$, decreases as $1/t$, due to Anderson localization. Eventually it saturates to the value set by metal absorption. b, Wavelength-resolved transmittance $T(\lambda)$ (red line) exhibits fluctuations. Color map: depth profile of average intensity $\langle I(x, y_0, z; \lambda) \rangle_x$ inside the slab at different wavelengths, highlighting spatially localized and necklace-like states.

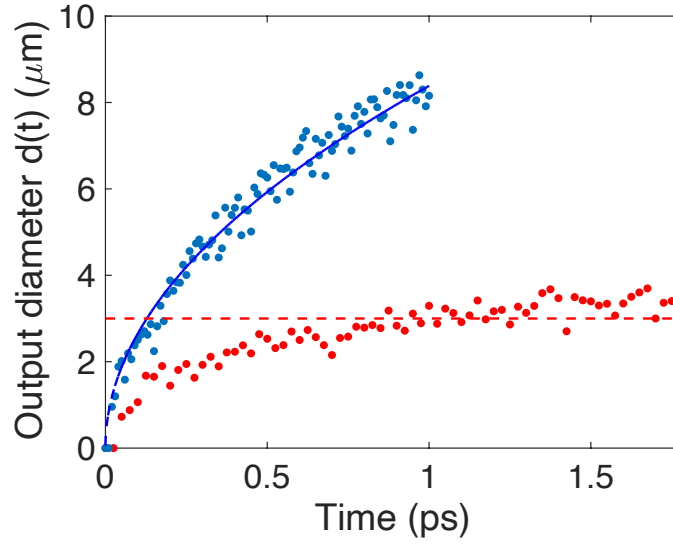


Figure S20: **Arrest of transverse spreading of visible light in 3D random aggregates of silver particles.** Transverse diameter of the transmitted light $d(t)$, with a tightly-focused incident pulse of center wavelength $\lambda_0 = 650$ nm, increases as \sqrt{t} in the diffusive slab ($f = 15\%$, blue dots) but it saturates to a constant value in the localized slab ($f = 48\%$, red dots). The slab thickness $L = 2$ μm . Silver spheres have radius $r = 50$ nm, $\sigma_0 \simeq 6.1 \times 10^7$ Ω^{-1}/m and $\tau \simeq 3.7 \times 10^{-14}$ s.